Science of the Total Environment 655 (2019) 482–511

Contents lists available at ScienceDirect

Science of the Total Environment

journal homepage: www.elsevier.com/locate/scitotenv

# Dryland changes under different levels of global warming

Aristeidis G. Koutroulis

*School of Environmental Engineering, Technical University of Crete, Greece*

## HIGHLIGHTS

- Dryland areas are vital ecosystems, highly sensitive to climatic changes.
- New higher resolution climate projections used to examine future aridity for RCP8.5
- The drylands could increase by an additional 7% of the global land surface by 2100.
- Up to 1.9 billion people could avoid living in drylands by keeping to 1.5 °C vs 4 °C.

## GRAPHICAL ABSTRACT

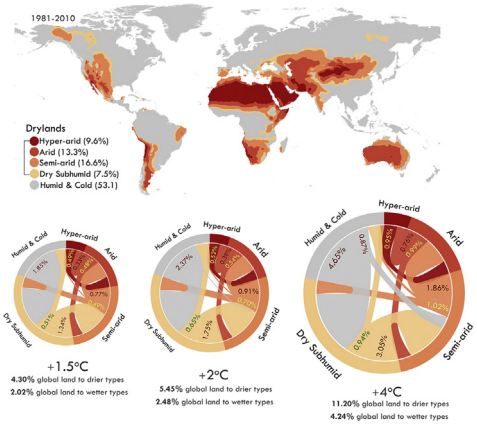


## ARTICLE INFO

*Article history:*
Received 14 September 2018
Received in revised form 13 November 2018
Accepted 14 November 2018
Available online 18 November 2018

*Keywords:*
Climate change
Aridity
Drylands
Water resources
Runoff
Global impacts

## ABSTRACT

Drylands are vital ecosystems which cover almost 47% of the Earth's surface, hosting 39% of the global population. Dryland areas are highly sensitive to climatic changes and substantial impacts are foreseen under a warming climate. Many studies have examined the evolution of drylands in the future highlighting the need for improved capability of climate models to simulate aridity. The present study takes advantage of new higher resolution climate projections by the HadGEM3A Atmosphere Global Climate Model using prescribed time varying SSTs and sea ice, provided by a range of CMIP5 climate models under RCP8.5. The aim of the higher resolution models is to examine the benefit of the improved representation of atmospheric processes in the dryland research and to see where these results lie in the range of results from previous studies using the original CMIP5 ensemble. The transient response of aridity from the recent past until the end of the 21st century was examined as well as the expansion of global drylands under specific levels of global warming (1.5 °C, 2 °C and 4 °C). Dryland changes were further assessed at the watershed level for a number of major global river basins to discuss implications on hydrological changes and land degradation. The areal coverage of drylands could increase by an additional 7% of the global land surface by 2100 under high end climate change. At a 4 °C warmer world above pre-industrial, 11.2% of global land area is projected to shift towards drier types and 4.24% to wetter. At the same level of warming the number of humans projected to live in drylands varies between 3.3 and 5.2 billion, depending on the socioeconomic developments. By keeping global warming levels to 1.5 °C, up to 1.9 billion people could avoid living in drylands compared to a 4 °C warmer world of low environmental concern.



*E-mail address:* koutroulis@hydrogaia.gr.

https://doi.org/10.1016/j.scitotenv.2018.11.215
0048-9697/

## 1. Introduction

Dryland areas extend over 47% of the terrestrial land surface and are inhabited by nearly 2.6 billion people. Despite being water-limited areas, over 43% of the global cropland area is located in drylands (Cherlet et al., 2018). Drylands are usually considered as fragile ecosystems, highly sensitive to climatic changes (Huang et al., 2016). They are closely linked with major threats in human and natural systems like water scarcity, land degradation, loss of net primary production, biodiversity decline and poverty (Daliakopoulos et al., 2016; Durán et al., 2018; Greve and Seneviratne, 2015; Williams et al., 2010). It is therefore of essential importance to advance the understanding of the underlying processes and improve the ability to project changes in drylands.

Dryland climatology is primarily controlled by interactions between general atmospheric circulation and regional topography (Nicholson, 2011) that affect atmospheric fluxes of precipitation and potential evapotranspiration. Besides these large scale processes, aridity is influenced by soil moisture feedbacks and plant physiological response to increasing $CO_2$ (Berg et al., 2016). Several recent studies improved our understanding on these key underlying mechanisms affecting dryland climate research (Berg et al., 2016; Greve et al., 2017; Gudmundsson et al., 2016; Huang et al., 2016; Scheff et al., 2015; Schlaepfer et al., 2017). Simplifications of the kind of "dry gets dryer" and "wet gets wetter" have been questioned by many researchers (Berg et al., 2016; Greve and Seneviratne, 2015; Roderick et al., 2015) and proved unconfirmed. This progress is largely based on a combination of improved information regarding observations, as well as climate model simulations over the past few years. The improvement in simulations is a result of increased modeling resolution and advanced parametrization of the physical processes leading to a more realistic representation of precipitation and temperature fields in terms of climate variability, long term trends and extremes (Knight et al., 2014; Koutroulis et al., 2016; Vautard et al., 2018). This progress improves the efficiency of simulating aridity and characterizing dryland changes in more detail.

Nevertheless, dryland climate research still faces major questions on the dynamic mechanisms that control changes in dryland climatology, such as land and ocean–atmosphere interactions and impacts of changes in atmospheric circulation over drylands, which need to be further investigated. Several studies have used the CMIP5 climate models, with a typical horizontal resolution of 100–200 km, to study the response of aridity to increasing greenhouse concentrations (Asadi Zarch et al., 2017; Feng and Fu, 2013; Huang et al., 2016; Huang et al., 2017a, b; Scheff et al., 2015; Schlaepfer et al., 2017), with contradicting results being reported. Differences are most apparent on the spatial response of wetting and drying patterns resulting to contradicting signals of dryland expansion and shrinkage in large areas like for example the Great Planes. Differences in dryland projections could most probably stem from several methodological differences like the selection of a subset of climate model simulations and differences in the adjustment of model biases (Koutroulis et al., 2018a, b), or even in the definition used to characterize drylands.

This study take advantage of new higher resolution climate projections by the HadGEM3A Atmosphere Global Climate Model using prescribed time varying SSTs and sea ice, provided by a range of CMIP5 climate models, forced with the RCP8.5 concentration scenario. The aim of this higher resolution model, with a horizontal resolution of roughly 60 km, is to examine the benefit of the improved representation of atmospheric processes in the dryland research and to see where these results lie in the range of results from previous studies using the original CMIP5 ensemble. As a first step the study examines the projected global mean precipitation, potential evapotranspiration and aridity changes with increasing global mean temperature as simulated by the ensemble of the new climate projections. A basic validation of the reference simulation is also performed by comparing aridity estimates based on observations and climate model simulations for the baseline period (1981–2010). The evolution of aridity for each dryland type (hyper-arid, arid, semiarid and dry-subhumid) and the global distribution of transitions towards drier or wetter conditions are then analyzed, along with the level of model agreement between the members of the climate model ensemble. Aridity changes are also compared to runoff changes at the basin level for 21 major global river basins. Runoff and evapotranspiration changes were further examined with the Budyko framework. Global scale and river basin scale changes in aridity were also assessed based on the number of people living in future dryland areas, considering either static population (2010 levels) or changing according to the socioeconomic projections (Socioeconomic Pathways — SSPs) at the time of passing the considered GWLs. Finally, avoided impacts are examined in terms of number of people that avoid living in drylands at a given level of global warming and socioeconomic scenario, compared to the worst case scenario developed in this study (RCP8.5-SSP3).

## 2. Material and methods

For the calculation of the aridity and the assessments with hydrological and socioeconomic changes a number of datasets and methods were used, described in following sections.

### 2.1. Climate observations

Global climate data of daily resolution developed by the Terrestrial Hydrology Group at Princeton University were used as observations for the present study (Sheffield et al., 2006). The second version of the dataset (PGFv2) is available for the 1901–2012 period at a global spatial resolution of 0.5°, including key near surface variables for terrestrial modeling. The PGFv2 is based on the NCEP-NCAR reanalysis dataset combined with station and satellite observations. Temperature and precipitation systematic biases are adjusted against CRU TS3.21, and shortwave and longwave radiation against a dataset developed by the University of Maryland (Müller Schmied et al., 2016b). The dataset has been extensively used in a number of global scale biophysical modeling experiments (Chang et al., 2017; Davie et al., 2013; Müller Schmied et al., 2016a; Veldkamp et al., 2017).

### 2.2. Global climate projections and warming levels

A set of higher resolution transient climate simulations was used, aiming for improved representation on natural variability and climate and thus aridity projections. Simulations were performed by the high-resolution atmosphere-only version (AGCM) of the HadGEM3A model (Hewitt et al., 2011; Walters et al., 2011). This next generation model with horizontal resolution of roughly 60 km at the equator (N216) is a transition version of those currently being used in upcoming CMIP6 experiments and is currently used by the UK Met Office in operationally global — long range seasonal and decadal forecasts. The model has been evaluated by Vautard et al. (2018) over Europe and, despite biases in several different processes, significant improvements were made in the representation of observed weather patterns.

Prescribed time varying Sea Surface Temperatures (SSTs) and Sea Ice Concentration (SIC) from a subset of CMIP5 climate models (Table 1)

**Table 1**
Time of passing global warming levels of 1.5, 2 and 4 °C in each bias corrected forcing from the hi-resolution climate simulations according to the RCP8.5 scenario.

| Model providing driving SSTs & SICs | Time of passing | | |
|---|---|---|---|
| | GWL1.5 | GWL2 | GWL4 |
| IPSL-CM5A-LR | 2024 | 2035 | 2071 |
| GFDL-ESM2M | 2036 | 2051 | n/a |
| HadGEM2-ES | 2019 | 2033 | 2071 |
| IPSL-CM5A-MR | 2023 | 2036 | 2069 |
| MIROC-ESM-CHEM | 2020 | 2032 | 2068 |
| ACCESS1-0 | 2026 | 2040 | 2081 |

under the RCP8.5 emission scenario were used as lower boundary conditions. The setup of prescribed SSTs and SIC form the CMIP5 models has the advantage of (a) the reduced computational effort compared to the expensive fully coupled atmosphere–ocean integrations and (b) the ability to compare the new results against those from other studies based on CMIP5 projections. The criterion to select the CMIP5 driving models was to cover the wider possible range of uncertainty in the future climate projections and thus to explore the maximum range of possible regional climate changes within limited computing resources (Wyser et al., 2016). The presence of systematic biases in climate model outputs limits their applicability (Grillakis et al., 2013). The adjustment of these biases against observations provide realistic and comparable impact assessments and improved understanding when examining the evolution of biophysical processes in the future projections, preferably when using methods that retain the long term trends and inter-annual variability (Grillakis et al., 2017). Therefore, climate model output variables were remapped in a common 0.5° × 0.5° grid and bias adjusted against the PGFv2 dataset (Sheffield et al., 2006) by applying a trend preserving bias adjustment method (Hempel et al., 2013). These new high resolution simulations have been used by a number of recent climate change impact studies (Alfieri et al., 2017; Betts et al., 2018; Dottori et al., 2018; Koutroulis et al., 2018a, b; Naumann et al., 2018; Shannon et al., 2018; Vousdoukas et al., 2018).

The present study of aridity changes was framed in terms of warming levels which are increasingly important due to their link with international climate policies (Jacob et al., 2012). Specific Global Warming Levels (GWLs) of 1.5 °C, 2 °C and 4 °C were defined based on transient global mean temperature projections resulting from RCP8.5 simulations relative to the preindustrial period (1870–1899 period). The year of passing a GWL was defined as the first time the 20-year running mean of the global averaged annual mean temperature gets above the GWL i.e. the year indicates the middle of a 20-year average. Future climate periods were then defined as 30-year time slices centered on the crossing year of the corresponding GWL. The baseline period was set to 1981–2010. The year that each GWL is surpassed varies between the members of the HADGEM3A ensemble. The year of GWL surpassing for each ensemble members is given in Table 1.

### 2.3. Aridity and potential evapotranspiration

Drylands are associated with the term of aridity, implying a permanent deficit of precipitation related to high evaporative demand. Aridity is most commonly measured by the Aridity Index (AI) defined as the ratio of cumulative annual precipitation (P) to the total potential evapotranspiration (PET). This water deficiency indicator is used to map drylands as regions for which $P/PET < 0.65$. Drylands are further classified into four categories (i) dry-subhumid ($0.5 \le AI < 0.65$), (ii) semi-arid ($0.2 \le AI < 0.5$), (iii) arid ($0.05 \le AI < 0.2$) and (iv) hyper-arid ($AI < 0.05$) (Huang et al., 2017a, b; Hulme, 1996). PET was calculated based on the Penman-Montieth method (Allen et al., 1998) which is considered as the most reliable method of estimating PET compared to other radiation and temperature based methods (Feng and Fu, 2013; Huang et al., 2016).

### 2.4. Global runoff simulation

The Joint UK Land Evrionment Simulator (JULES) land surface model was driven by the bias adjusted climate model ensemble on a global grid resolution of 0.5° (Papadimitriou et al., 2016) to produce runoff simulations. JULES is the land surface scheme of the Met Office Unified Model that can also be used as a standalone model. It simulates fluxes through different processes such as the hydrological and carbon cycles, the surface exchange of energy, vegetation and plant physiology and others (Best et al., 2011). JULES has the advantage of including the process of the plant physiological response to increasing $CO_2$, an important process which is often neglected in "pure" global hydrological models, leading to more severe drying (Betts et al., 2015; Milly and Dunne, 2016; Swann et al., 2016). A more detailed description of the JULES model setup used in this study is given by Papadimitriou et al. (2017).

### 2.5. Population projections

Changes in aridity were also assessed with respect to affected population. Population density was either considered static at the levels of 2010 or assumed to change according to projections consistent with specific Shared Socioeconomic Pathways (SSPs) (Jones and O'Neill, 2016) at the time period around the time of passing each GWL (Table 1). Therefore, population density at a specific GWL varies for each ensemble member as a result of the different time of reaching this GWL. Differences between urban and rural population changes were also taken into account to identify patterns of change for the different SSPs. The spatial distribution and the size of population at the year 2010 and at each GWL was obtained by the spatially explicit population scenarios consistent with the SSPs (Jones and O'Neill, 2016) at a horizontal resolution of 7.5 arc min, globally.

The RCP8.5 scenario can be combined with specific SSPs whose narratives are plausible with increased emission rates, especially for the higher warming level (GWL4) considered in this study. Three SSPs were considered for assessment as plausible combinations with RCP8.5. The SSP3 is a regional rivalry scenario assuming high population growth rates for high fertility countries and the opposite for low fertility. Urbanization in the case of SSP3 is slowly evolving. Combined with RCP8.5 emissions and biophysical impacts it can be considered as a scenario with high challenges for adaptation that can be closely compared to a "no adaptation option". The SSP2 is characterized as the middle of the road with medium challenges for adaptation and moderate growth and urbanization rates. Finally, SSP5 is a fossil-fueled development scenario but with low adaptation challenges with low population growth and fast demographic transitions.

## 3. Results

The first step of the study is the examination of projected global mean precipitation, potential evapotranspiration and aridity changes with increasing global mean temperature as simulated by the ensemble of the new climate projections. A basic validation of the reference simulation by comparing aridity estimates based on observations and climate model simulations for the baseline period, follows. The evolution of aridity for each sub-type and the global distribution of transitions are analyzed. Aridity changes are also compared to runoff changes at the basin level for 21 major global river basins. Finally, changes in aridity were assessed with respect to the number of people living in future dryland areas considering either static (2010 levels) or changing according to the SSPs projections at the time of passing the considered GWLs.

### 3.1. Climate model simulations

The comparison of the high resolution climate model simulations with the original CMIP5 show good spatial agreement (Wyser et al., 2016). The benefits of higher resolution are noticeable on regional scales. For example, the representation of precipitation features associated with orographic rainfall is improved and temperature patterns and magnitudes are depicted more realistically, as a result of the more detailed underlying topography. The improvement in the simulation of climate variables has a direct impact on the realistic representation of aridity. Fig. 1 summarizes the response of the global land only mean precipitation change, the global mean potential evapotranspiration as calculated by the Penman-Montieth algorithm based on the outputs of the climate model and the global mean aridity index against global mean temperature change. Temperature anomalies are relative to preindustrial levels (1870–1899) and vary between the members of the climate model ensemble. At the higher end of each of the simulation the

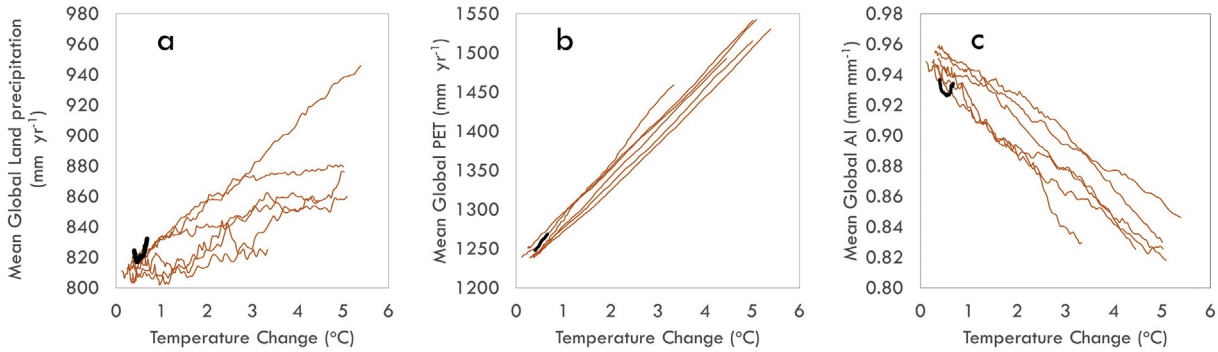


**Fig. 1.** (a) Projected global land only mean precipitation change (mm $yr^{-1}$), (b) global mean potential evapotranspiration (mm $yr^{-1}$) and (c) global mean aridity index (mm $mm^{-1}$) against global mean temperature change. Values are 20 yr running means between 1971 and 2130. Changes in temperature are relative to pre-industrial (1870–1899). All projections are HadGEM3 simulations driven with RCP8.5. Black lines correspond to observations (PGFv2).

20 yr running mean of temperature increase ranges between 3.3 °C (GFDL-ESM2M) and 5.4 °C (MIROC-ESM-CHEM) as a response to increased greenhouse gases. Global mean precipitation over land is simulated to increase with temperature. The rate of increase varies between the ensemble members, ranging from 844 mm/yr (GFDL-ESM2M) and 946 mm/yr (MIROC-ESM-CHEM). Potential evapotranspiration shows a clear linear increasing response with increasing global temperature. The rate of increase is similar for all ensemble members and the higher end response varies between 1459 mm/yr (GFDL-ESM2M) and 1543 mm/yr (IPSL-CM5A-LR).

### 3.2. Reference simulations of aridity

Fig. 2 presents the global distribution of total drylands and dryland sub-categories as calculated based on observations for the 1981–2010 baseline period. Based on these estimates 46.9% of total land area is characterized as drylands according to the definition (P/PET < 0.65), from which 9.6% are classified as hyper-arid, 13.3% arid, 16.6% semi-arid and 7.5% dry-subhumid. This calculation takes into account the actual land area fraction of each grid cell considering the change in size by latitude. This can lead in different estimates with studies which do not account for the actual extent of land area. The spatial distribution and the classification of drylands are in close agreement with previous, recent studies (Asadi Zarch et al., 2017; Cherlet et al., 2018; Daliakopoulos et al., 2017; Feng and Fu, 2013; Huang et al., 2017a, b; Scheff et al., 2015). A direct comparison of the aridity values at grid cell level as derived by observations (PGFv2) versus the bias adjusted simulations are shown in Fig. 2b. The axes of the scatterplot are constrained to aridity index values < 0.65, corresponding to drylands, and it is evident that observed aridity values are highly replicated by the bias adjusted outputs of the climate model simulations. According to aridity values based on climate model simulations for the baseline period, there is a slight difference of +0.5% of global land area compared to observed aridity. Deviations are also present in the dryland subcategories with the greatest being observed in the hyper-arid category. Observations denote a fraction of 9.6% while simulations 10.9% of global land area. This difference could be attributed to the remaining biases in some of the variables used for the calculation of PET, resulting to higher PET estimate and as a consequence lower AI values. These areas are mostly detected at both sides of the Indus river: the Thar Desert at the borders between India and Pakistan and the wider area of Central Brahui Range in Pakistan, the south and southwest edges of Rub' Al Khali Desert in Yemen and the south edges of Sahara desert. These areas are simulated as hyper-arid by the climate models and as arid regions based on observations. The differences in the other categories are negligible.

### 3.3. Projections of aridity

#### 3.3.1. Transient global mean changes

Changes in precipitation and potential evapotranspiration from a changing climate have a direct impact on the extent of the drylands. Fig. 3 illustrates the areal extent for total drylands and the corresponding sub-categories for the recent past and the future projections from both climate model simulations and observations. The total area of global drylands for the recent past is estimated to 63.4 × $10^6$ $km^2$

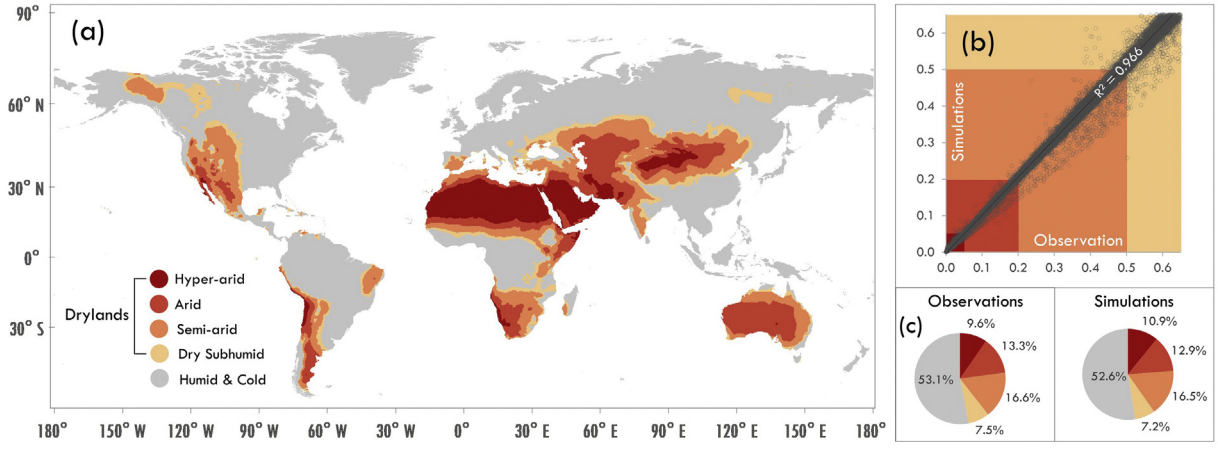


**Fig. 2.** (a) Global distribution of drylands based on observations (reanalysis combined with station and satellite observations) for the 1981–2010 baseline period. (b) Scatter plot of aridity index calculated from observations against bias corrected climate model simulations for the baseline period. The diagram is constrained to aridity index values < 0.65 (drylands). (c) Areal coverage (percentage) of drylands per category in the form of pie charts as calculated from observations and simulations for the baseline period.

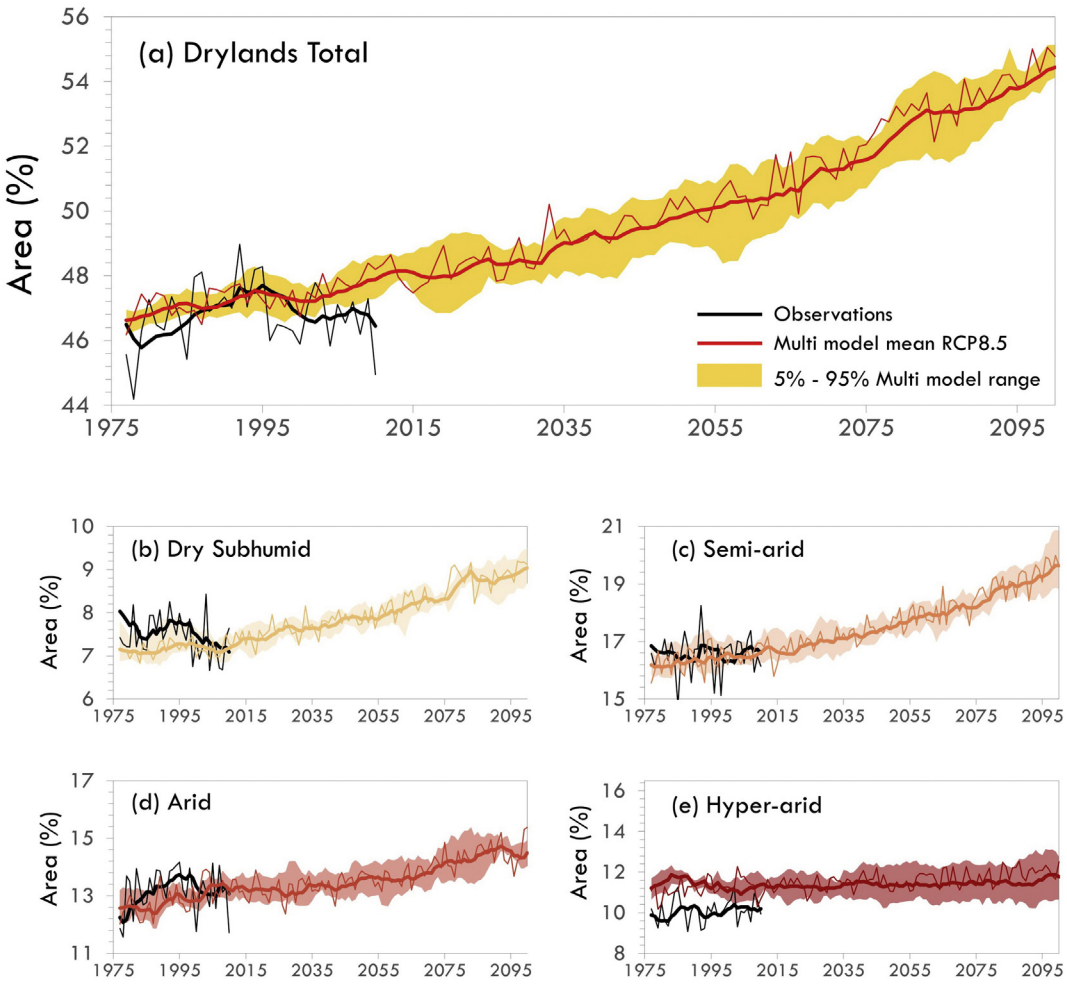


**Fig. 3.** Areal extent (fraction of global land area) for (a) total drylands (AI < 0.65), (b) dry-subhumid (0.5 ≤ AI < 0.65), (c) semi-arid (0.2 ≤ AI < 0.5), (d) arid (0.05 ≤ AI < 0.2) and (e) hyper-arid regions (AI < 0.05). Black lines correspond to observations (PGFv2). Colored lines are baseline and RCP8.5 multi-model mean simulations. Shaded area is the 5%–95% multi-model range. Thin lines correspond to annual values while thick lines to 7-yr running means.

(46.9% of the global land) and $64 \times 10^6$ km$^2$ (47.4% of the global land) based on observations and climate models, respectively. Despite these differences the ensemble of climate model runs can robustly simulate an expansion of the drylands. Their area is projected to increase by $9.3 \times 10^6$ km$^2$ (or 6.9% of the global land) by the end of the 21st century according to the RCP8.5. The pattern of expansion is also robust for all sub-categories except the hyper-arid, which shows a slight increase by $0.8 \times 10^6$ km$^2$ (or 0.6% of the global land). This is the dryland type with the largest difference in simulation between observations and climate model runs, as explained in the previous section. The type with the maximum areal change is the semi-arid which is foreseen to expand by $4.3 \times 10^6$ km$^2$ (or 4.3% of the global land). This expansion shows a stronger trend for the second half of the 21st century. Dry-subhumid type has the second largest increase (by $2.5 \times 10^6$ km$^2$ or 1.9% of the global land), followed by arid expanse (by $1.7 \times 10^6$ km$^2$ or 1.3% of the global land).

*3.3.2. Regional patterns of changes at specific global warming levels*

Several transitions are expected to be triggered by precipitation and potential evapotranspiration changes due to a fast warming climate (RCP8.5). Fig. 4 summarizes these transitions towards drier or wetter types at the specific GWLs. The magnitude of changes increases with global warming. For 1.5 °C global warming the changes are not clearly evident as the spatial distribution of transitions is patchy. Changes to drier types are limited along the border regions of the current drylands (1981–2010). Western north America, southern Africa, the northern borders of western and eastern Asia drylands, Mediterranean and Australia are the regions that include areas moving to drier states at 1.5 °C global warming (Fig. 4a). Transition to wetter conditions are foreseen for a few areas of south Asia and middle eastern Asia with a notable change from semi-arid and dry-subhumid to humid conditions over northeast India. For 2 °C global warming the changes are more pronounced. The patchy spatial pattern gives its place to well-formed transects of increasing or decreasing aridity. These transects are obvious for central North America, central Asia and eastern Europe in which changes from dry-subhumid to semi-arid and from semi-arid to arid, dominate. Wetting patterns appear similar to the warming level of 1.5 °C. For 4 °C global warming extensive patterns of changes clearly arise. Dryland of the central North America expand eastward transforming massive areas of the Great Plains from humid to dry-subhumid and semi-arid. East European and west Asian drylands expand massively northwards. Transects of increased aridity are also

**Fig. 4.** Global distribution of projected drylands transitions according to RCP8.5 for the three GWLs, relative to the baseline (1981–2010) period. Brown colored areas denote transition to drier types and green colored areas transitions to wetter types. Grey shaded areas are drylands of the baseline period. Box whiskers on the right denote the mean and the range of the areal extend for each subtype transition (drier or wetter) from the multi-model projections.

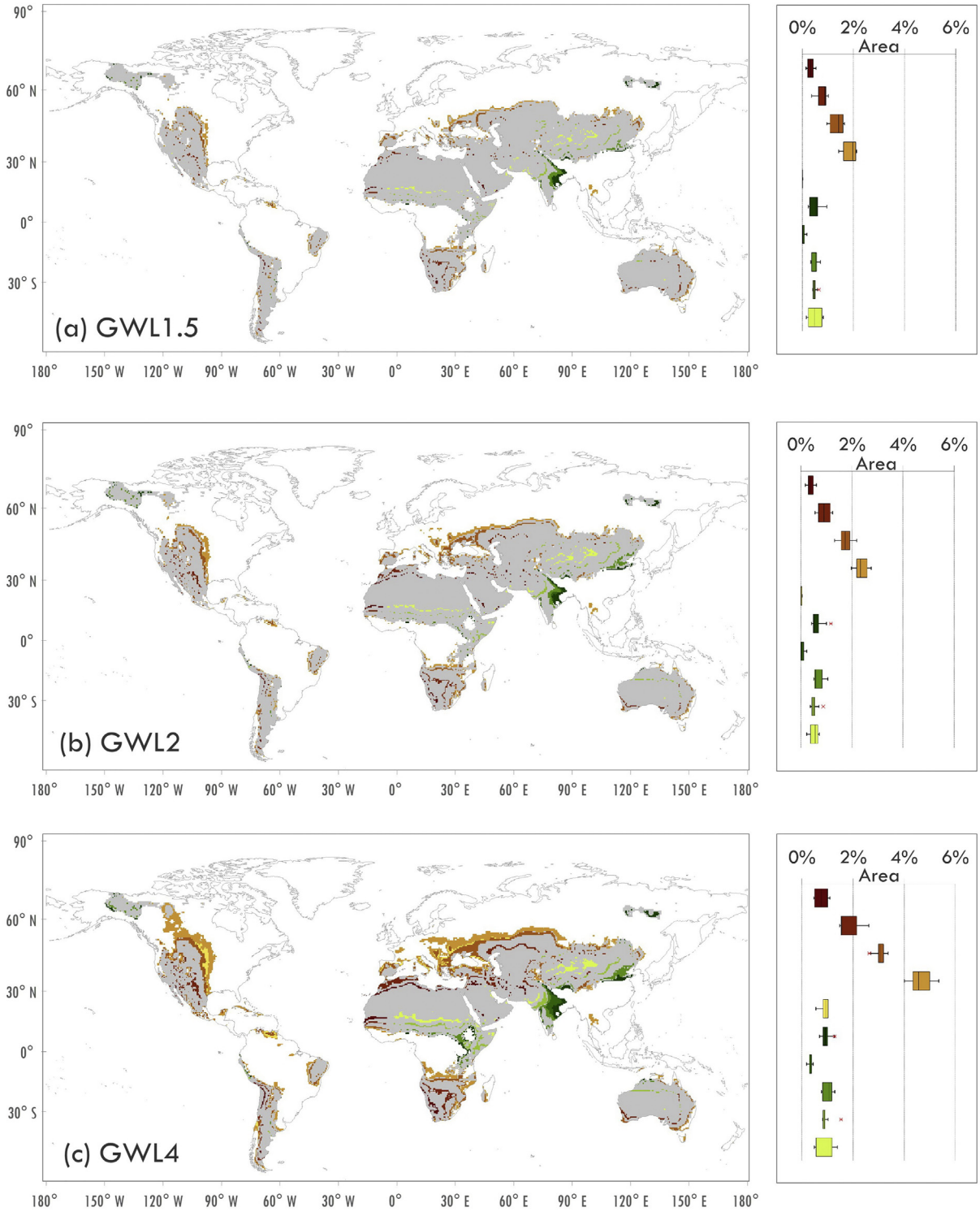
90°
60° N
30° N
0°
30° S
(a) GWL1.5
180° 150° W 120° W 90° W 60° W 30° W 0° 30° E 60° E 90° E 120° E 150° E 180°
0% 2% 4% 6%
Area
(b) GWL2
(c) GWL4
Transition to drier types
Arid → Hyper-arid
Semi-arid → Arid
Dry Subhumid → Semi-arid
Humid → Dry Subhumid
Humid → Semi-arid
Dry Subhumid → Humid
Semi-arid → Humid
Semi-arid → Dry Subhumid
Arid → Semi-arid
Hyper-arid → Arid
Transition to wetter types

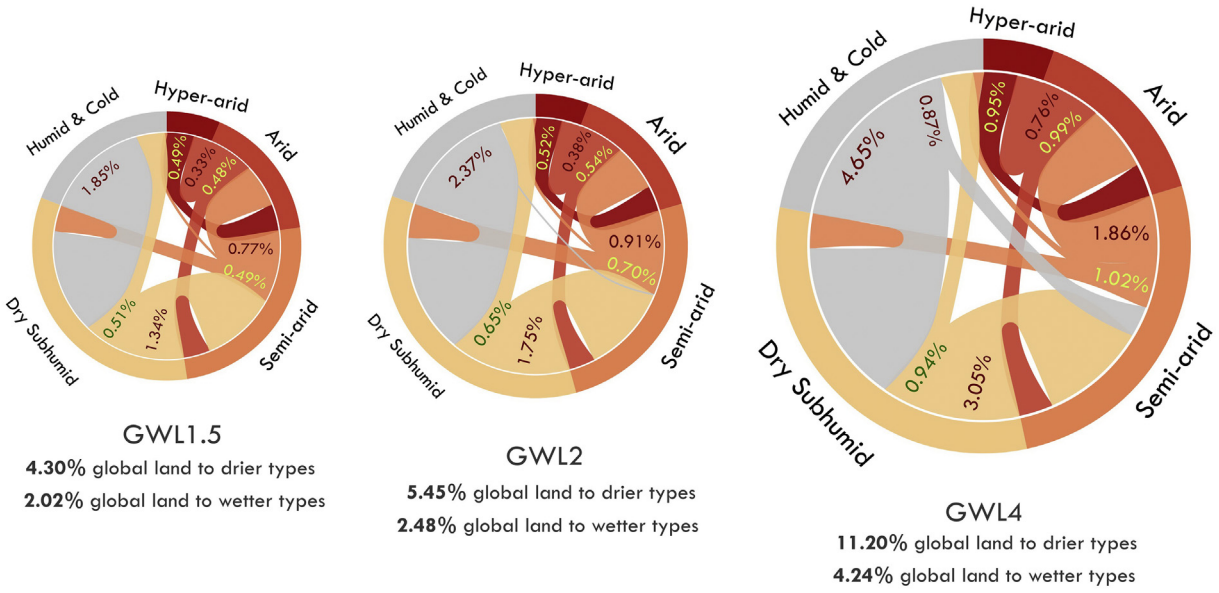


**Fig. 5.** Areal extent (fraction of global land area) of projected transitions in each dryland sub-category under the three GWLs. The size of the chord diagrams is proportional to the total areal extend of the global land changing to drier or wetter types. Percent changes to drier types are marked in red and to wetter in green.

notable over southern European countries, north and south Africa and Australia. In contrast, strong wetting patterns are simulated over north India, middle and east China, the Horn of Africa and over the arid steppes and desert areas south of Sahara. The projected areal extend of transitions to drier and wetter types are relatively highly robust between the members of the climate model ensemble as illustrated by the box-whiskers on the right parts of Fig. 4. The accompanying appendix includes figures (Fig. A2 for GWL1.5, Fig. A3 for GWL2 and Fig. A4 for GWL4) similar to Fig. 4 but illustrating projected transition separately for each member of the climate model ensemble. Fig. 5 summarizes the areal extent of projected transitions (drying and wetting) in each dryland sub-category under the three GWLs as simulated by the climate model ensembles. At 1.5 °C global warming transition to drier types are simulated for 4.3% of the global land area compared to the recent past conditions. For the higher levels of global warming of 2 °C and 4 °C the dryland areas are expanding to 5.45% and 11.2%, respectively. On the other hand, 2.02% of the global land area shows a wetting trend at 1.5 °C, growing to 2.48% at 2 °C and to 4.24% at 4 °C. The most significant drying trend in terms of areal coverage is the transition from humid to dry-subhumid, which is over 40% of the overall drying areas for all the considered global warming levels. Changes towards drier conditions predominate over drying changes ending up to a global expansion of drylands, sprawling with increased global warming.

CMIP5 climate models used to drive the HADGEM3A model have highly different responses in their projections. Therefore, the examination of the consensus between the members of this climate model ensemble is important. Fig. 6 shows the global distribution of multi model agreement on the sign of change for the three GWLs considered in this study. For 1.5 °C global warming the change in the spatial pattern of the level of agreement is not evident (scattered distribution). Model agreement of the order of 100% towards drier types is obtained only for 0.19% of the global land area. For a world at 2 °C global warming and for 100% level of agreement, a global land area of 0.69% is projected to shift to drier states. This area is limited at the borders of the south and southeast European drylands, surrounded by drier projected areas of lower model agreement. Similarly for the eastern borders of North American drylands, while for south Africa the distribution is scattered. At the 4 °C global warming level clear patterns of high model agreement towards drier and wetter conditions can be distinguished. All models agree towards drier conditions for the 4.73% of the global land area. These regions span over the Great Plains area, north Venezuela, and the rain shadow areas eastern of Andes, Chile, for America continent. Vast areas west and north of the Black Sea connected with a transect extending to north of Kazakhstan are robustly projected to get drier. Spain, south France, Italy and Greece also appear to get drier at GWL4 with a high model consensus, along with north Morocco and Algeria. Transects of drying signals are also surrounding Kalahari Desert over south Africa. Australian drylands are expected to expand southwards. On the contrary, north and central India, areas over eastern and north desert areas of China, north of Lake Victoria over South Sudan, Kenya and Somalia and transects south of Sahara desert are robustly projected to be wetter in a world at 4 °C global warming.

The abovementioned changes in aridity are triggered by changes in precipitation and potential evapotranspiration as a response global warming. Fig. A1 of the appendix includes changes in precipitation and potential evapotranspiration for the three specific GWLs relative to the baseline (1981–2010). Potential evapotranspiration has a spatially robust increasing signal globally except the northern India area at the warming levels of 1.5 °C and 2 °C. The reduction in PET over India could be attributed to oversaturated atmospheric conditions. Precipitation has a much more diverse but spatially robust signal which is getting stronger with higher global temperatures. Decrease in precipitation combined with increase in PET leads to increased aridity and expansion of drylands for many regions identified previously (Great Plains, Mediterranean, South Africa). There are also regions like the Amazon that despite the projected severe decrease in precipitation and increase in PET, especially at the GWL4, it is still classified as humid with a spatially averaged, multi-model mean aridity index value of 1.31 (at GWL4). On the other hand precipitation is foreseen to increase for large parts of the world. A representative example is north India, for which projected precipitation increases combined with reduced PET, lead to reduced aridity and shrinkage of drylands.

### 3.4. Human population and dryland changes

Drylands of today as estimated in this study (1981–2010) extent over 46.9% of the land surface and are home to 38.8% of the global population (2010 levels). Climate models result to a fraction of 39.2% (range

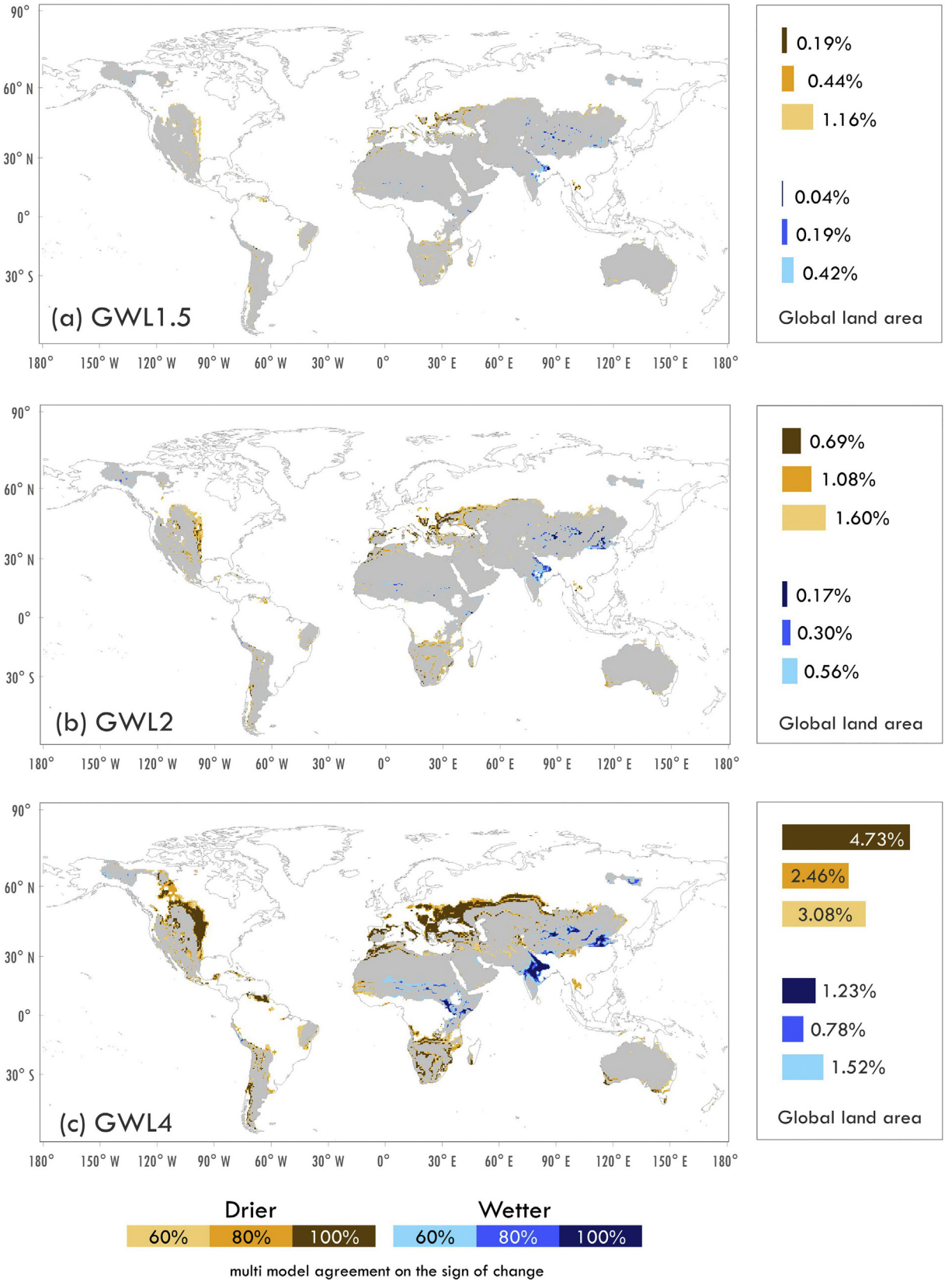


**Fig. 6.** Global distribution of multi model agreement on the sign of change for the three GWLs. Bar graphs on the right denote the areal extend (fraction of global land area) falling under a specific level of agreement of transitions to drier or wetter aridity states.

from 38.6% to 40%) for the same estimate. Fig. 7 shows the number of people living in dryland areas for total drylands, dry-subhumid, semi-arid, arid and hyper-arid regions for the baseline period and based on climate model projections at the time of reaching the GWLs, considering static population at the levels of 2010 or assuming a population change according to projections consistent with specific SSPs. Global population

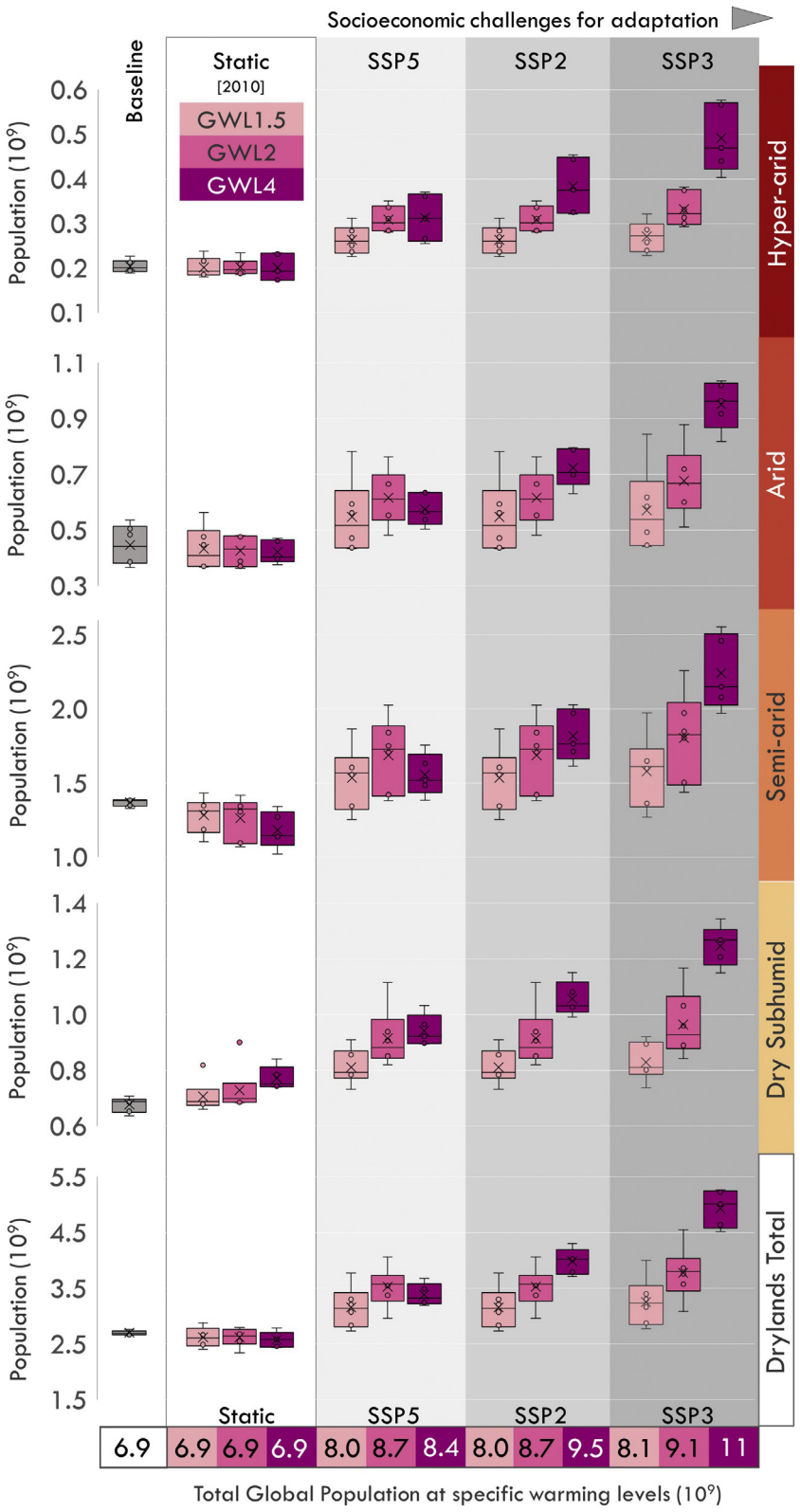


**Fig. 7.** Number of people living in dryland areas for total drylands, dry-subhumid, semi-arid, arid and hyper-arid regions for the baseline period and based on climate model projections at the time of reaching the GWLs, considering static population at the levels of 2010 or assuming to change according to projections consistent with specific SSPs. Total global population at the time of reaching each GWL and for each SSP is denoted at the lower part of the figure.

from 6.9 billion in 2010 is expected to increase between 8.0 and 8.1 billion at a global warming level of 1.5 °C depending on the assumed socioeconomic projection (SSP5, SSP2 or SSP3) at the time that each individual member passes the GWL1.5 (ranging between 2019 and 2036 — Table 1). At 2 °C (2032–2051) global population will increase to an expected range from 8.7 (SSP5 and SSP2) to 9.1 billion (SSP3), while at 4 °C (2068–2081) global population varies between 8.4 (SSP5) and 11.2 (SSP3) billion.

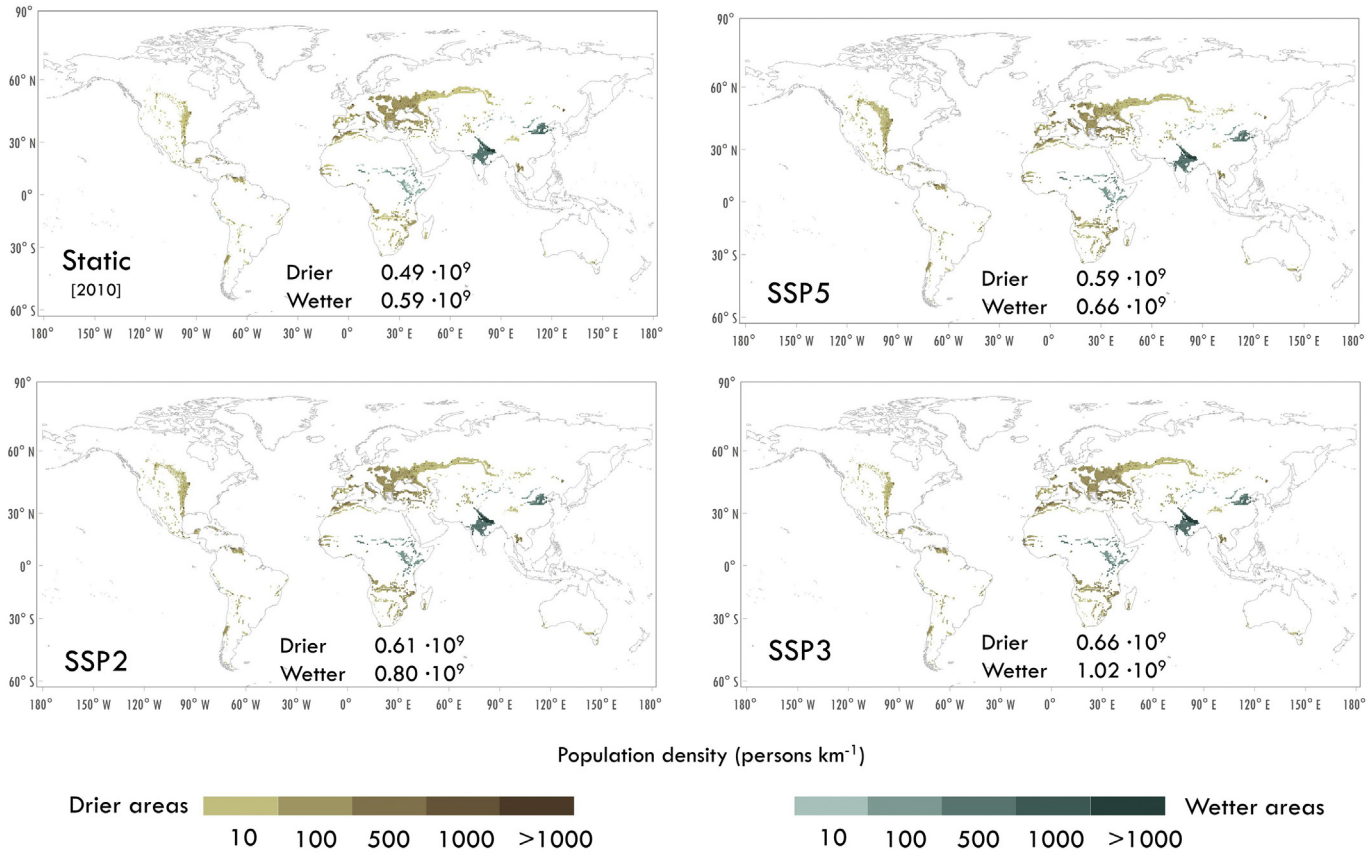


**Fig. 8.** Population density of areas shifting to drier or wetter conditions for the GWL4. Population either considered static or changing according to the SSPs. Projected population densities are masked by areas with over 80% level of agreement on the sign of drier or wetter change.

Expanding drylands under global warming combined with increases in population leads to a highly vulnerable future world with a number of implications related to increasing aridity: water scarcity and desertification. The increase in vulnerability does not just depend on the magnitude of changes but critically relies on the spatial patterns of aridity and population changes and the socioeconomic conditions of this population, in combination. If no population change is assumed (static 2010 levels) a slight decrease of people living in dryland areas is projected for all warming levels by 76, 77 and 121 million people, at 1.5 °C, 2 °C and 4 °C, respectively. Although the areal coverage of drying regions are consistently larger than the coverage of the wetting regions, for every level of global warming, population density in wetting areas is higher. This is clearly seen in Fig. 8 for example in which population density of areas shifting to drier or wetter conditions for the GWL4 are masked by areas with over 80% level of agreement on the sign of drier or wetter change. At GWL4, 80% of the models agree that 7.19% of the global land will shift to drier conditions and 2.01% to wetter (Fig. 6) but 121million fewer people will be exposed to dryland because wetting is taking place in the highly populated regions of India and China. Considering a changing population according to the low growth SSP5 scenario, the number of people living in drylands are shaped to 0.46 (0.07 to 1.02) billion at 1.5 °C, 0.83 (0.30 to 1.31) billion at 2 °C and 0.70 (0.53 to 0.96) billion at 4 °C (Fig. 7). Furthermore different urbanization rates are projected under the different socioeconomic developments. Although population growth is slow for SSP5, the demographic transitions are rapid. Figs. A5 and A6 of the appendix are similar to Fig. 7 but splitting total population to rural and urban. The high urbanization rate is notable for SSP5 especially at the time of passing GWL4

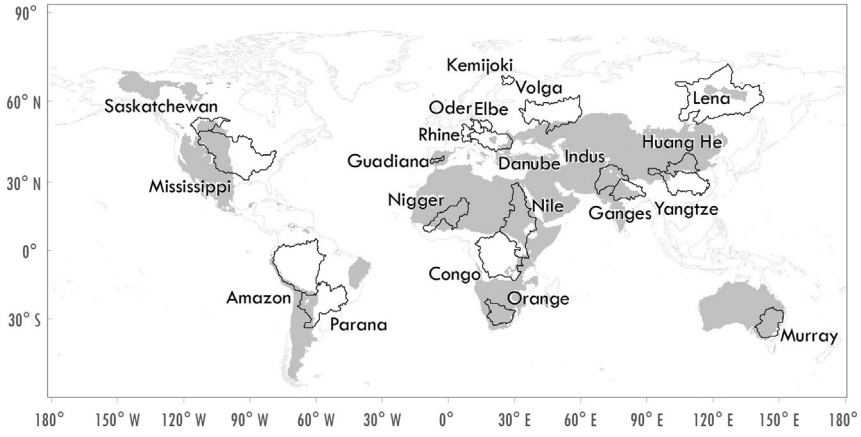


**Fig. 9.** Location of the 21 major global river basins considered in this study. Grey shaded regions correspond to drylands of the baseline (1981–2010) period.

**Table 2**
Major global river basins characteristics (size, population density, mean annual runoff) and absolute and relative changes in mean annual runoff for the three GWLs.

| | Basin | Hydrobelt (Meybeck et al., 2013) | Size ($10^6$ km$^2$) | Population density (persons/km$^2$) | Multi model mean annual runoff (mm) | Runoff change (mm) | | | Relative Runoff change (%) | | |
|---|---|---|---|---|---|---|---|---|---|---|---|
| | | | | | | GWL1.5 | GWL2 | GWL4 | GWL1.5 | GWL2 | GWL4 |
| 1 | Amazon | Equator | 4.70 | 5 | 912 | −63 | −72 | −141 | −7% | −8% | −15% |
| 2 | Congo | Equator | 3.72 | 28 | 302 | 0 | −6 | 47 | 0% | −2% | +15% |
| 3 | Mississippi | North mid-latitude | 3.24 | 26 | 161 | 3 | 1 | 4 | +2% | 0% | +3% |
| 4 | Nile | North dry | 2.95 | 51 | 163 | 6 | 10 | 51 | +4% | +6% | +31% |
| 5 | Lena | Boreal | 1.51 | 1 | 45 | 11 | 8 | 36 | +25% | +17% | +80% |
| 6 | Parana | South subtropical | 2.50 | 29 | 288 | 24 | 40 | 108 | +8% | +14% | +38% |
| 7 | Yangtze | North mid-latitude | 1.67 | 214 | 277 | 7 | 25 | 88 | +2% | +9% | +32% |
| 8 | Volga | North mid-latitude | 1.35 | 46 | 78 | −2 | −2 | 7 | −2% | −3% | +8% |
| 9 | Murray | South mid-latitude | 1.06 | 1 | 102 | −1 | 6 | 16 | −1% | +6% | ++15% |
| 10 | Niger | North subtropical | 1.38 | 18 | 86 | 6 | 2 | 18 | +7% | +2% | 21% |
| 11 | Orange | South dry | 0.89 | 16 | 55 | −1 | 0 | 3 | −1% | −1% | +6% |
| 12 | Ganges | North mid-latitude | 0.94 | 518 | 296 | 125 | 189 | 589 | +42% | +64% | +199% |
| 13 | Indus | North mid-latitude | 0.97 | 231 | 95 | 14 | 12 | 43 | +15% | +12% | +46% |
| 14 | Danube | North mid-latitude | 0.81 | 100 | 223 | −11 | −18 | −26 | −5% | −8% | −12% |
| 15 | Huang He | North mid-latitude | 0.72 | 139 | 56 | 8 | 13 | 32 | +14% | +23% | +57% |
| 16 | Rhine | North mid-latitude | 0.18 | 271 | 443 | −4 | −19 | −38 | −1% | −4% | −9% |
| 17 | Elbe | North mid-latitude | 0.13 | 169 | 82 | 2 | −1 | 4 | +2% | −2% | +5% |
| 18 | Oder | North mid-latitude | 0.10 | 157 | 76 | 2 | 0 | 4 | +3% | −1% | +5% |
| 19 | Guadiana | North mid-latitude | 0.07 | 23 | 95 | −4 | −8 | −15 | −5% | −8% | −15% |
| 20 | Kemijoki | Boreal | 0.06 | 3 | 116 | 20 | 28 | 67 | +17% | +24% | +58% |
| 21 | Saskatchewan | Boreal | 0.39 | 9 | 73 | 3 | 2 | 2 | +4% | +3% | +3% |

(2068–2081). The increased migration to urban areas combined with drylands expansion result to substantial higher levels of urban population exposed to drylands at 4 °C, despite the concurrent reduction of total global population. Apart from the total drylands, Fig. 7 (and Figs. A5 & A6) also illustrate population information for the dryland subtypes. The most populated type is the semi-arid followed by dry-subhumid. Considering the pure effect of population changes (for given aridity changes meaning the comparison between SSPs and static [2010] in Fig. 7) at a 1.5 °C warmer world, semiarid (dry-subhumid) regions are foreseen to be inhabited by another 0.25 (0.11) billion people shaping total population for these dryland types to 1.53 (0.81) billion. This increase is exaggerated at 2 °C by 0.42 (0.19) billion people and reduced to 0.37 (0.17) billion due to decreases in global population according to SSP5 assumptions, corresponding to a total 1.69 (0.94) billion at 2 °C and to 1.56 (0.94) billion totally. For the moderate socioeconomic scenario SSP2 the changes at 1.5 °C and 2 °C are similar to SSP5. However, at 4 °C a significant increase by 1.4 billion (total 3.98 out of 9.45) people living in drylands is foreseen based on socioeconomic projections. Urbanization in SSP2 is also apparent but not as strong as in SSP5. For the "no adaptation" scenario (SSP3-RCP8.5) global drylands are projected to be inhabited by an additional 0.63 (0.37 to 1.12) billion (total 3.25 out of 8.12) at 1.5 °C, 1.16 (0.74 to 1.76) billion (total 3.78 out of 9.08) at 2 °C and 2.35 (4.93 to 11.25) billion people at 4 °C.

### 3.5. Changes at the basin scale

Aridity changes were further assessed against runoff changes at basin scale for 21 major global river basins (Fig. 9). These river basins cover a wide range of the heterogeneous global hydrological regimes (Meybeck et al., 2013) and have a diverse extent of dryland in the baseline or the projection period. Table 2 includes basin characteristics regarding their size, the population density, the mean annual runoff as well as absolute and relative changes in mean annual runoff for the

**Table 3**
Mean aridity index (spatially and temporally averaged) and dryland extent of the 21 river basins for the baseline period and projected changes for the three GWLs.

| | Basin | Multi model mean aridity index (1981–2010) (mm mm$^{-1}$) | Aridity change (mm mm$^{-1}$) | | | Fraction of drylands | | | |
|---|---|---|---|---|---|---|---|---|---|
| | | | GWL1.5 | GWL2 | GWL4 | Baseline | GWL1.5 | GWL2 | GWL4 |
| 1 | Amazon | 1.67 | −0.12 | −0.17 | −0.39 | 7% | 7% | 7% | 26% |
| 2 | Congo | 1.02 | −0.04 | −0.05 | −0.08 | 8% | 10% | 11% | 28% |
| 3 | Mississippi | 0.79 | −0.07 | −0.11 | −0.22 | 42% | 46% | 48% | 63% |
| 4 | Nile | 0.33 | 0.00 | 0.01 | 0.04 | 84% | 84% | 84% | 83% |
| 5 | Lena | 1.04 | 0.04 | 0.03 | 0.03 | 4% | 4% | 4% | 19% |
| 6 | Parana | 0.87 | 0.00 | 0.00 | −0.02 | 28% | 28% | 29% | 44% |
| 7 | Yangtze | 1.11 | −0.03 | −0.04 | −0.08 | 10% | 11% | 11% | 28% |
| 8 | Volga | 1.08 | −0.10 | −0.14 | −0.29 | 8% | 13% | 15% | 41% |
| 9 | Murray | 0.32 | −0.02 | −0.02 | −0.02 | 93% | 94% | 94% | 96% |
| 10 | Niger | 0.22 | 0.00 | 0.01 | 0.00 | 90% | 90% | 91% | 94% |
| 11 | Orange | 0.22 | −0.02 | −0.02 | −0.05 | 97% | 99% | 99% | 99% |
| 12 | Ganges | 0.55 | 0.11 | 0.14 | 0.37 | 71% | 54% | 50% | 41% |
| 13 | Indus | 0.31 | 0.01 | 0.01 | 0.01 | 91% | 91% | 91% | 94% |
| 14 | Danube | 1.13 | −0.13 | −0.20 | −0.36 | 18% | 30% | 36% | 61% |
| 15 | Huang He | 0.42 | 0.02 | 0.03 | 0.06 | 90% | 87% | 86% | 86% |
| 16 | Rhine | 1.72 | −0.13 | −0.22 | −0.43 | 0% | 0% | 0% | 17% |
| 17 | Elbe | 0.97 | −0.07 | −0.13 | −0.22 | 0% | 0% | 4% | 38% |
| 18 | Oder | 0.87 | −0.08 | −0.14 | −0.23 | 0% | 0% | 14% | 69% |
| 19 | Guadiana | 0.42 | −0.06 | −0.08 | −0.15 | 100% | 100% | 100% | 100% |
| 20 | Kemijoki | 1.62 | 0.03 | 0.01 | −0.04 | 0% | 0% | 0% | 17% |
| 21 | Saskatchewan | 0.68 | −0.03 | −0.06 | −0.16 | 50% | 58% | 65% | 87% |

three GWLs, simulated by the JULES model. The size of the basins varies from the boreal Kemijoki basin of $60 \times 10^3$ km$^2$ to the equatorial Amazon of $4.7 \times 10^6$ km$^2$ modeled area. Mean annual runoff ranges from 45 mm of equivalent precipitation for the boreal Lena basin to 912 mm for the Amazon basin. The response of runoff to global warming varies substantially between the members of the climate models ensemble (Betts et al., 2018). There is a general tendency towards increased runoff with global warming with the largest increase to be simulated for Ganges basin with a model consensus of higher flows by +42%, +64% and +199% at GWL1.5, GWL2 and GWL4, respectively (Table 2). There is also a high level of model agreement of reduced runoff for Amazon, Guadiana and Danube by up to −15% at GWL4.

Table 3 includes details on the mean aridity index and the dryland extent of the 21 river basins for the baseline period and the projected changes for the three GWLs.

Although runoff is increasing for most of the basins (with a few exceptions), aridity is mainly higher for the majority of them. The most severe increase in aridity (decrease of aridity index in Table 3) is estimated for Rhine basin at 4 °C global warming, resulting in the classification of 17% of its area as dryland compared to the lack of drylands for the baseline period, the GWL1.5 and the GWL2. Climate models, on the contrary, project increasingly lower aridity for Ganges lessening dryland extent from 71% during the baseline to 54% (1.5 °C), 50% (2 °C) and 41% (4 °C). Besides Rhine, the European basins Elbe, Oder and Kemijoki are the ones with 0% dryland extend during the baseline and the GW1.5 and this is projected to drastically change for the GWL of 2 °C and especially of 4 °C. Oder and Danube and Elbe are the basins with the largest expansion of drylands. Being also highly populated areas, vulnerability to risks relating to higher aridity like water scarcity, land cover changes and degradation is also increasing. Table 4 includes population density information at the river basin scale for the 1981–2010 period and projected relative changes according to the different socioeconomic pathways (SSP2, SSP3 and SSP5) at the time of passing the three GWLs. Ganges is the most densely populated basin followed by Rhine which, however have a contrasting population growth pattern amongst the SSPs. For Ganges a general increasing population signal is assumed by all SSPs (at a different degree) but for Rhine population is projected to be lower than baseline for SSP3, roughly similar for SSP2 and higher for SSP5.

Fig. 10 illustrates the comparison of projected relative changes in mean runoff against aridity changes, for the 21 major global river basins under the three GWLs. The mean aridity index for each basin is also denoted by the relative size of the symbols. Substantial changes in runoff are projected concurrently with changes in aridity. At 1.5 °C the simulated changes have a mixed signal of aridity and runoff response. There are basins (Amazon, Danube, Rhine, Volga Guadiana) for which higher aridity (lower aridity index) is associated with lower mean flows on average. For other basins (Ganges, Lena, Kemijoki, Huang He) lower aridity is accompanied by increased runoff. However, for a number of basins (Oder, Elbe, Yangtze, Saskatchewan) simulations show increase in both aridity and runoff at the same time. At 2 °C of warming the simulated changes are similar to 1.5 °C while for 4 °C the runoff–aridity relationship is shifted towards higher (positive) runoff and lower aridity with the increase of global warming and the range of changes expanding. Most of the examined basins appear to have the concurrent response of increased runoff and aridity with implications with respect to soil erosion and land degradation.

Runoff and aridity changes were further examined at the grid point scale for the 21 global river basins to reveal regional responses within the watershed boundaries. Fig. 11 illustrates the distribution of changes in runoff against aridity changes for each grid point of the corresponding river basin, under the three GWLs. Furthermore, changes in aridity index of each GWL against the aridity of the baseline period for each grid point of the corresponding river basin are also included, highlighting positive and negative runoff changes and magnitude of changes in the same plot. Fig. 11 shows results for the Mississippi, the Nile and the Ganges basins while results for the rest of the basins are included in the appendix (Figs. A7 to A12). The analyzed major river basins span over areas of various hydro-climatic regimes, thus having a range of runoff responses to changes in aridity. The Mississippi basin shows a general increasing aridity signal with global warming (Table 3) yet mean runoff is projected to be relatively unchanged when looking at the spatially aggregated multi-model mean. Zooming in, the runoff responses vary from positive to negative when looking at the grid point level (Fig. 11). The range of the changes is between −200 mm and +200 mm compared to the spatially averaged mean annual runoff of 161 mm. The magnitude of runoff changes is larger for the energy limited points of the basin and the opposite for the water limited. The threshold between the energy and water limited areas is the value of aridity index = 1 in the vertical axis, thus a horizontal line intersecting at 1 with the vertical axis. This is visually distinguishable for several river basins spanning both energy and water limited areas, like

**Table 4**
Basin scale population information at the year 2010 scale and projected relative changes according to the different socioeconomic pathways at the time of passing the three GWLs.

| | Basin | Population density 2010 (persons/km$^2$) | Relative population changes | | | | | | | | |
|---|---|---|---|---|---|---|---|---|---|---|---|
| | | | SSP5 | | | SSP2 | | | SSP3 | | |
| | | | GWL1.5 | GWL2 | GWL4 | GWL1.5 | GWL2 | GWL4 | GWL1.5 | GWL2 | GWL4 |
| 1 | Amazon | 5.5 | 6% | 5% | −12% | 13% | 20% | 21% | 13% | 40% | 81% |
| 2 | Congo | 27.9 | 40% | 70% | 116% | 46% | 85% | 168% | 46% | 101% | 228% |
| 3 | Mississippi | 25.6 | 17% | 33% | 87% | 11% | 19% | 37% | 11% | 6% | −5% |
| 4 | Nile | 50.8 | 33% | 56% | 89% | 39% | 72% | 142% | 39% | 87% | 211% |
| 5 | Lena | 0.7 | −6% | −9% | −21% | −5% | −8% | −18% | −5% | −7% | −8% |
| 6 | Parana | 28.7 | 9% | 12% | 0% | 13% | 19% | 19% | 13% | 27% | 47% |
| 7 | Yangtze | 213.6 | −2% | −7% | −35% | 1% | −3% | −28% | 1% | 1% | −17% |
| 8 | Volga | 46.0 | 1% | 1% | −6% | 0% | −1% | −3% | 0% | −4% | −2% |
| 9 | Murray | 1.4 | 35% | 69% | 167% | 25% | 44% | 82% | 25% | 20% | 14% |
| 10 | Niger | 17.9 | 40% | 70% | 118% | 51% | 98% | 218% | 51% | 125% | 336% |
| 11 | Orange | 16.3 | 16% | 27% | 36% | 14% | 23% | 34% | 14% | 18% | 33% |
| 12 | Ganges | 517.6 | 15% | 23% | 19% | 20% | 33% | 47% | 20% | 45% | 94% |
| 13 | Indus | 230.5 | 20% | 30% | 31% | 26% | 46% | 76% | 26% | 62% | 143% |
| 14 | Danube | 99.7 | −1% | −1% | −3% | −2% | −4% | −16% | −2% | −8% | −24% |
| 15 | Huang He | 139.5 | 2% | −1% | −26% | 3% | 1% | −22% | 3% | 3% | −14% |
| 16 | Rhine | 271.4 | 6% | 13% | 33% | 2% | 3% | 1% | 2% | −7% | −29% |
| 17 | Elbe | 169.1 | 6% | 12% | 30% | 1% | 2% | −2% | 1% | −8% | −32% |
| 18 | Oder | 156.9 | 4% | 7% | 12% | 1% | −1% | −12% | 1% | −9% | −35% |
| 19 | Guadiana | 23.0 | 0% | 3% | 17% | 1% | −1% | −12% | 1% | −3% | −28% |
| 20 | Kemijoki | 2.6 | 10% | 20% | 57% | 5% | 9% | 17% | 5% | −2% | −15% |
| 21 | Saskatchewan | 9.0 | 25% | 50% | 129% | 17% | 31% | 61% | 17% | 13% | 4% |


**Fig. 10.** Projected relative changes in mean runoff (%) against aridity changes (mm mm$^{-1}$) for the 21 major global river basins under the three GWLs. The values correspond to spatially averaged multi-model mean aggregates at the basin scale. The size of the circles is proportional to the areal average — temporal mean value of the aridity index at the specific GWL.

Mississippi (Fig. 11), Amazon and Congo (Fig. A7), Parana and Yangtze (Fig. 8A) and others. A signal transition zone for runoff, from positive to negative and vice versa, can be clearly identified for all river basins, when looking in aridity changes. This transition is apparent in the space of negative aridity changes (increased aridity). The greater the increase in aridity, the higher the tilt of the transition zone relative to the vertical axis. The fraction of area with this behavior (positive runoff change despite the increase in aridity) vary between the river basins but is apparent for most of them and this is attributable to the combined effect of several factors that drives the hydrological behavior.

The basin scale responses of annual water and energy balances to a changing climate were also examined through their changes in the Budyko space (Budyko, 1974). The Evaporative Index (actual evapotranspiration over precipitation — AET/P) was calculated based on the AET output from JULES model and the bias corrected precipitation simulated by the climate model runs (and used to drive JULES). The Dryness Index (potential evapotranspiration over precipitation — PET/P) is the inverse of the Aridity Index used to characterize drylands in the present study. Fig. 12 shows the annual water and energy balances of the 21 major global river basins plotted in the Budyko space for the baseline period and the three GWLs. It has to be noted that a single river basin could span over a range of diverse hydroclimatic regimes yet there are mapped in the Budyko space based on their spatially averaged water and energy balances. Several basins are classified as energy limited basins (Rhine, Amazon, Kemijoki, Danube, Yangtze, Volga, Lena and Congo) based on their climatic characteristics during the baseline period. Global warming triggers a substantial movement towards the water limiting threshold for all these basins and as a result three of them, Danube, Volga and Congo passes the marginal value of Dryness Index = 1 even with a global warming of 1.5 °C moving to the water limited space according to the Budyko hypothesis. Nile, Murray, Niger, Orange and Indus are classified amongst the most water limited basins (Orange with DI = 5.7 at 4 °C is not shown within the range of SWL4 in the Fig. 12). According to the Budyko assumption on the partitioning of precipitation to AET and water yield (here defined as runoff), the larger the change in the Dryness Index (Fig. 12) the higher the fraction of precipitation that turns to AET and hence the less the water yield (water available for runoff). Such a behavior can be observed for the warming levels of 1.5 °C and 2 °C for which in combination with the increase in the Evaporative Index, mean runoff is increasing in response to a reduction of the Dryness Index. However, this assumption is not true for the higher level of warming (4 °C). For several basins, positive changes in aridity are associated to increased runoff and this can be attributed to the impact of increasing levels of $CO_2$ on plant water use. Especially for basins with a large extend of humid areas (energy-limited environments) it is expected that the plant physiological response to elevated $CO_2$ will lead to reduced transpiration and a subsequent increase in runoff (Roderick and Farquhar, 2011). JULES model used to calculate AET and runoff is able to simulate these processes.

The basin-scale aridity response to a changing climate was also examined from the perspective of affected population. Table 4 includes population information of the recent past (2010) and projected relative changes according to the different socioeconomic pathways at the time of passing the three GWLs. Ganges basin is by far the most highly populated basin (over 500 people per km$^2$) and at a 4 °C world its population is expected to increase by 19% (SSP5) to 94% (SSP3). At the same time, Ganges is projected to respond with an overall increase in aridity, but on the contrary a substantial increase in runoff and a reduction in dryland extent, making local population less vulnerable to increasing aridity and water scarcity. The majority of European basins will be less populated than today at a 4 °C warmer world assuming a scenario of regional rivalry (SSP3). On the contrary, African basins are projected to have the highest increase in population. Fig. 13 shows relative population changes (%) for each SSP against the mean at the specific GWLs for the 21 major global river basins. It can be noted that population increases with the level of global warming as a consequence of the temporal evolution of the increasing global population patterns. Higher population growth is expected to take place in dryer basins and this is even more pronounced for higher levels of global warming. Expansion of drylands and population growth will exacerbate the vulnerability to freshwater scarcity and land degradation.

## 4. Discussion and conclusions

Recent assessments of observed and projected aridity improved our understanding on dryland research, irrespective of their contradicting findings regarding the definition of dryness and its spatial and temporal evolution (Dai, 2011; Greve et al., 2017, 2014; Greve and Seneviratne, 2015; Naumann et al., 2018; Sheffield et al., 2012; Trenberth et al., 2014). Despite this recent progress, dryland climatology still faces major challenges on understanding the dynamic mechanisms of dryland climate change (Huang et al., 2017a, b). This understanding largely

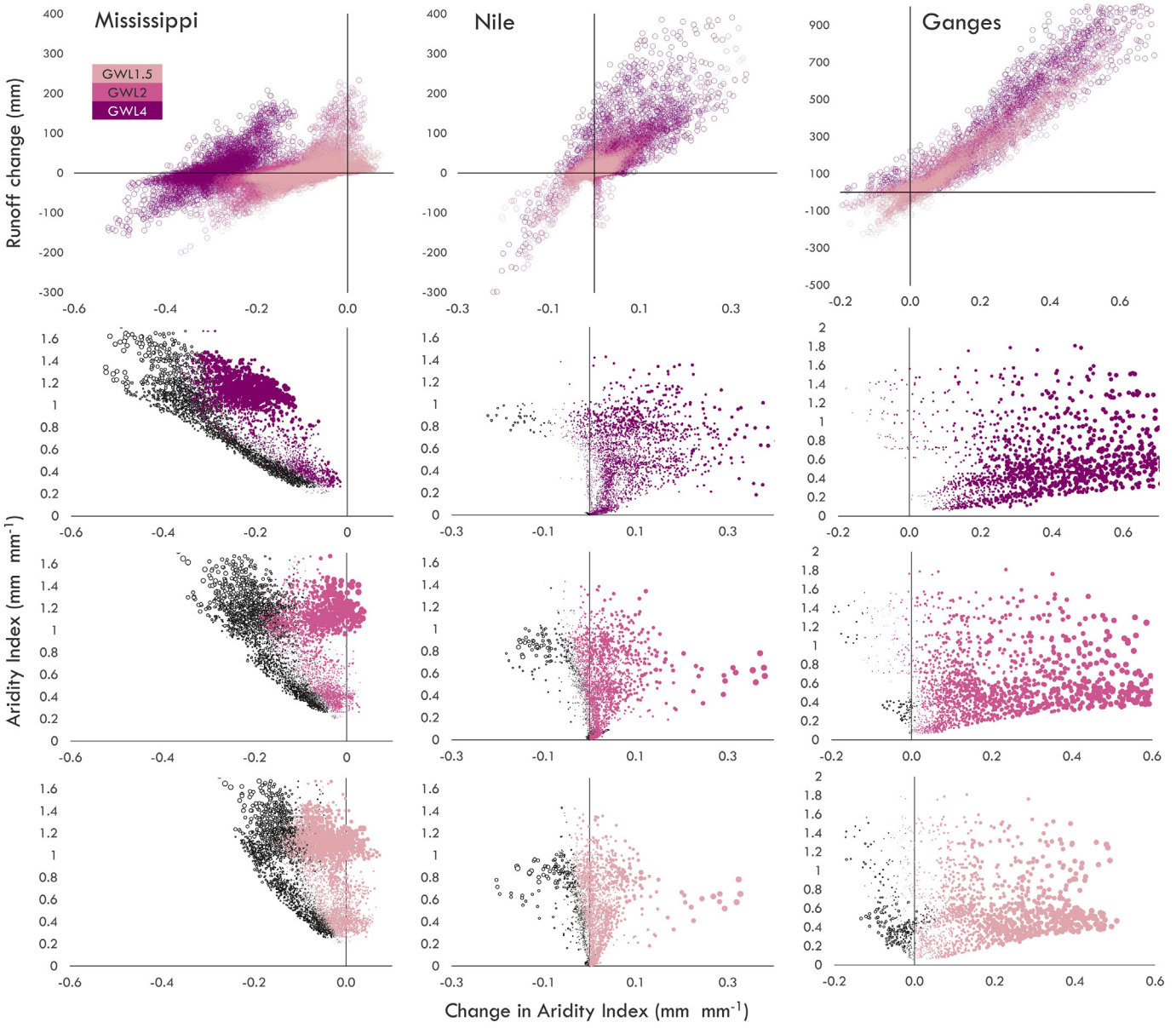


**Fig. 11.** (upper row panels) Distribution of runoff changes (mm) against aridity changes (mm $mm^{-1}$) for each grid point and for each member of the multi-model ensemble of the corresponding river basin under the three GWLs. (lower panels) Changes in aridity index (mm $mm^{-1}$) of each GWL against aridity of the baseline period for each grid cell of the corresponding river basin. Colored dots denote positive runoff changes and black dots negative runoff changes. The size of the dot is proportional to the magnitude of the change in runoff relative to the baseline period.

relies on the ability of climate simulations to realistically reproduce dynamical and physical processes. It is well known that despite the global trends of temperature can be fairly simulated, there is a lack of agreement on global precipitation patterns which is even more exaggerated at the regional level (Deser et al., 2017). The model uncertainty is by far the dominant factor of uncertainty compared to internal variability and scenario uncertainty (Hawkins and Sutton, 2011). Furthermore, the adjustment of inherent biases is inevitably applied in several impact studies with the risk of trends alteration and distortion of physical consistency between basic variables like temperature and precipitation. However, the climate model community is striving to achieve significant advancements and despite the models being far from perfect, the improvement is clear over time. The simulations used in the present study were performed by HadGEM3A model. It is currently one of the highest resolution global models used in weather and climate research. This new set of higher resolution climate simulations with improved representation on natural variability and climate were used to study the transient response of aridity under the RCP8.5 concentration scenario. Even though a single atmosphere model is used there is a consistent picture of drying and wetting patterns, comparable with other studies based on large model ensembles (CMIP5). The results of the study indicate that the recent areal coverage of drylands (47%) could increase by an additional 7% of the global land surface by 2100 under high end climate change. At the global warming level of 4 °C above preindustrial, 11.2% of global land area is simulated to shift towards drier types and 4.24% to wetter. At the same level of warming the number of humans projected to live in drylands varies between 3.3 and 5.2 billion, depending on the socioeconomic developments. Much of the dryland expansion will take place in developing countries. Aridity changes were also examined at the watershed scale for 21 global river basins. It was found that although runoff is increasing for most of the basins (with a few exceptions), aridity is mainly higher for the majority of them. For several basins, positive changes in aridity are associated to increased runoff which is in line with recent studies (Berg et al., 2016;

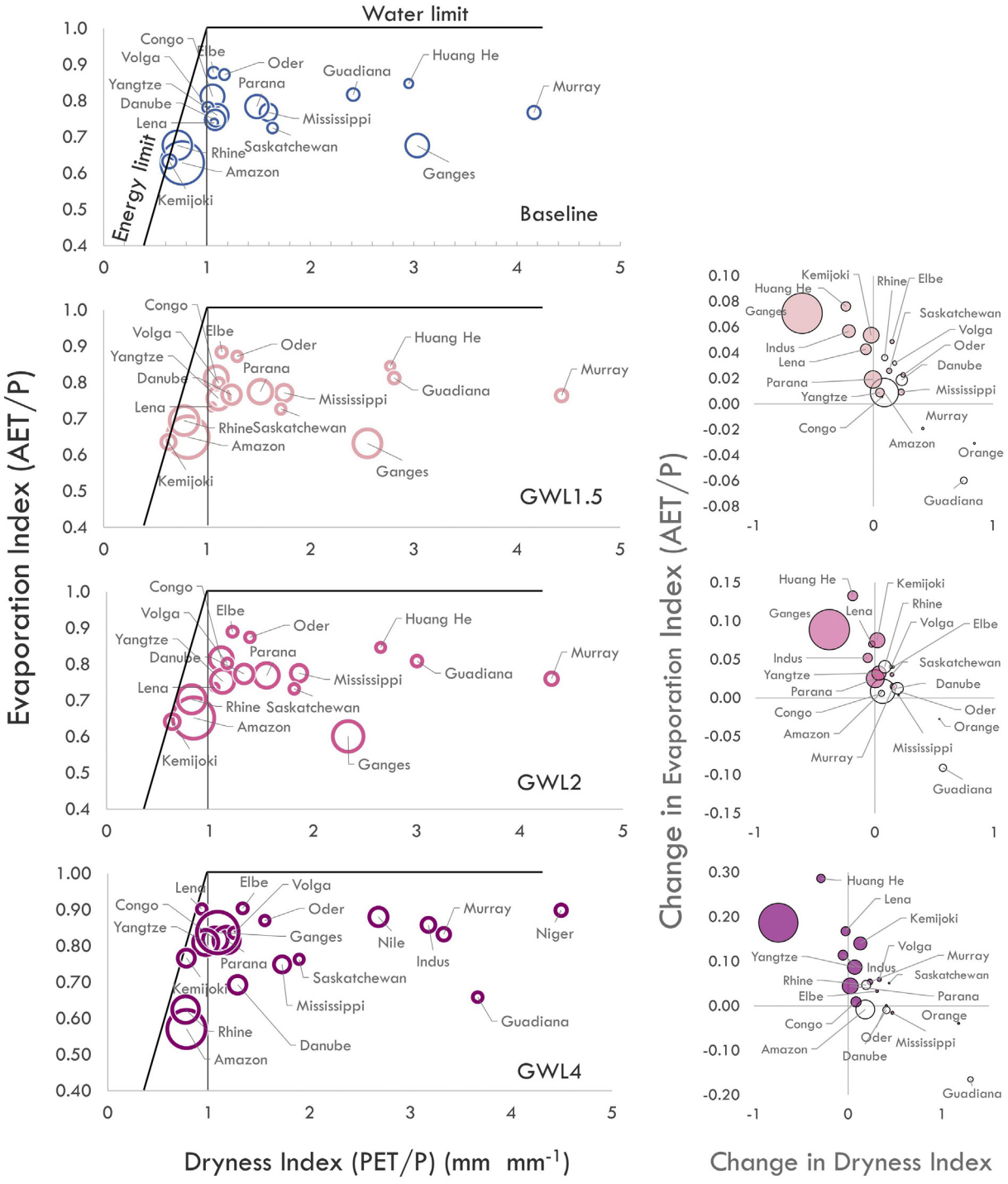


**Fig. 12.** (Column 1): Annual water and energy balances of the 21 major global river basins plotted in the Budyko space for the baseline period and the three GWLs. Energy limited basins are considered those with Dryness Index (PET/P) values < 1 and water limited basins have Dryness Index values > 1. The size of the symbols is proportional to mean annual runoff at each GWL. (Column 2): Projected changes of water and energy balances for each GWL. The size of the symbol is proportional to the value of change in runoff from the baseline (Table 3). Color symbols denote positive runoff changes and black circles negative.

Betts et al., 2015; Milly and Dunne, 2016; Swann et al., 2016). It is important to distinguish terrestrial aridity modeled by the AI index and hydrological aridity using surface runoff. A recent study (Yang et al., 2018) examined continental scale past and future trends concluding that increase in AI does not necessarily mean decrease in surface runoff. The latter is more sensitive to precipitation changes compared to potential evapotranspiration changes and as a result small relative increase in precipitation can prevail over evapotranspiration increase. This can be further attributed to the enhanced plant water use efficiency due to $CO_2$ fertilization, notably for basins with a large extend of humid areas (energy-limited environments) in which reduced transpiration could lead to increase in runoff. This concurrent response of increased runoff and aridity could probably lead to increased risk of land degradation and desertification especially under changing soil temperature regimes (Borrelli et al., 2017; Grillakis et al., 2016; Panagos et al., 2015).

A weakness of the present study is the use of a single atmosphere model and a single land surface model that constrains the capturing of

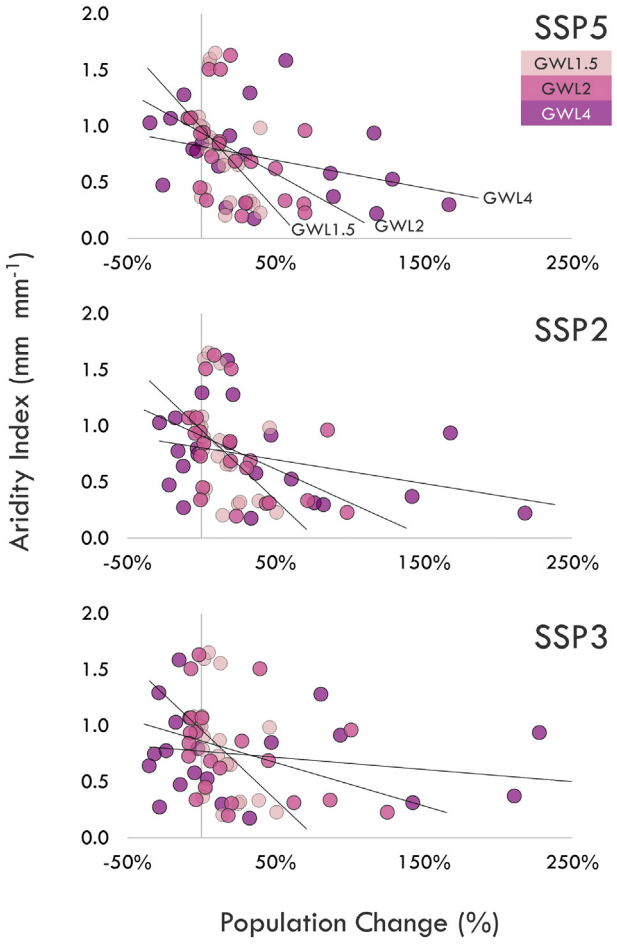


**Fig. 13.** Relative population changes (%) for each SSP against areal average — temporal mean value of the aridity index (mm $mm^{-1}$) at the specific GWLs for the 21 major global river basins. The level of population is defined according to the SSP projections at the time of reaching the specific GWL.

the full range of uncertainties. However the high resolution AGCM was driven by boundary conditions from a subset of CMIP5 and simulations show good spatial agreement, magnitudes and patterns of change with the CMIP5 (Wyser et al., 2016). Moreover, the model is capable of reproducing extreme weather patterns (Vautard et al., 2018). A second limitation, that is a significant drawback in Earth system sciences, is the lack of spatiotemporal homogeneity in climate variables of the global observation datasets (Trenberth et al., 2014) which constrains realistic estimates of evapotranspiration, one of the basic parameters for modeling aridity. Besides observations, climate model simulations are not free from biases, necessitating the use of methods for adjusting these biases. Bias corrected projections, and thus future aridity estimates, are sensitive to the conceptualization of the underlying methods. For example, the findings of the present study regarding the spatial patterns of dryland expansion have substantial similarities with Feng and Fu (2013) and differences with the study by Huang et al. (2016). Despite the fact that both of these two studies are based on the same PET dataset, they project contrasting signals of changes. In more detail, Huang et al., 2016 foresees transition to wetter conditions over the Great Plains in contrast to Feng and Fu, 2013 that simulate extensive drying. These differences can be atributed to the different methodologies used to correct systematic biases and also different observational datasets.

Special focus should be given to the benefits of keeping global temperature rise at 1.5 °C above preindustrial levels compared to higher levels of warming. This information is extremely relevant to mitigation and adaptation climate policies consistent with the goals set by Paris Agreement (Jacob et al., 2018; United Nations, 2016). According to this study 6.9% (1.15%) of the global terrestrial surface will keep away from transiting to dryer aridity types by staying at 1.5 °C global warming compared to a 4 °C (2 °C) world. Furthermore, roughly 2.7 billion people are currently living in drylands (year 2010) and this number is expected to rise to a total of 5.2 billion at a 4 °C global warming, according to the worst case SSP3-RCP8.5 scenario. Fig. 14 summarizes the avoided impacts in terms of number of people that avoid drylands inhabiting compared to the worst-case GWL4 RCP8.5-SSP3 scenario. Comparing 1.5 °C versus 2 °C impacts on human population approximately 0.4 billion for SSP5 & SSP2 and 0.5 billion for SSP3 will avoid dryland habitation. Avoided impacts are more significant when comparing 1.5 °C versus 4 °C. In summary, by keeping global warming levels to 1.5 °C, up to 1.9 billion people could avoid living in drylands compared to a 4 °C warmer world of low environmental concern (RCP8.5-SSP3).

High resolution climate simulations indicate that changes towards drier conditions predominate over wetter changes under the RCP8.5 scenario, ending up to a global expansion of drylands. This expansion in combination with increasing population will exacerbate the vulnerability to freshwater scarcity, land degradation & desertification and therefore food security and poverty. Future exposure of humans to expanding drylands can be avoided by appropriate climate mitigation policies and proactive adaptation actions linked to the Sustainable Development Goals.

## Acknowledgements

Part of the research leading to these results has received funding from the European Union Seventh Framework Programme FP7/2007–2013 under grant agreement no 603864 (HELIX: High-End cLimate Impacts and eXtremes; www.helixclimate.eu). The HadGEM3A simulations were performed at the Met Office Hadley Centre.

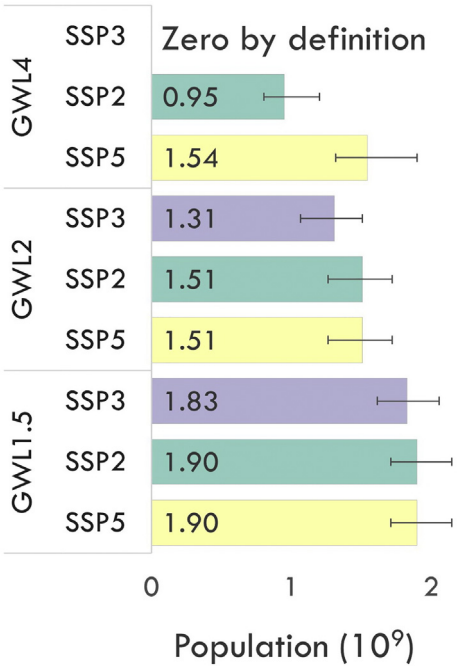


**Fig. 14.** Number of people avoid dryland inhabiting compared to the worst-case GWL4 RCP8.5-SSP3 scenario. Values are global mean population (across ensemble members) according to the SSPs projections at the time of passing the specific GWLs.

## Appendix A

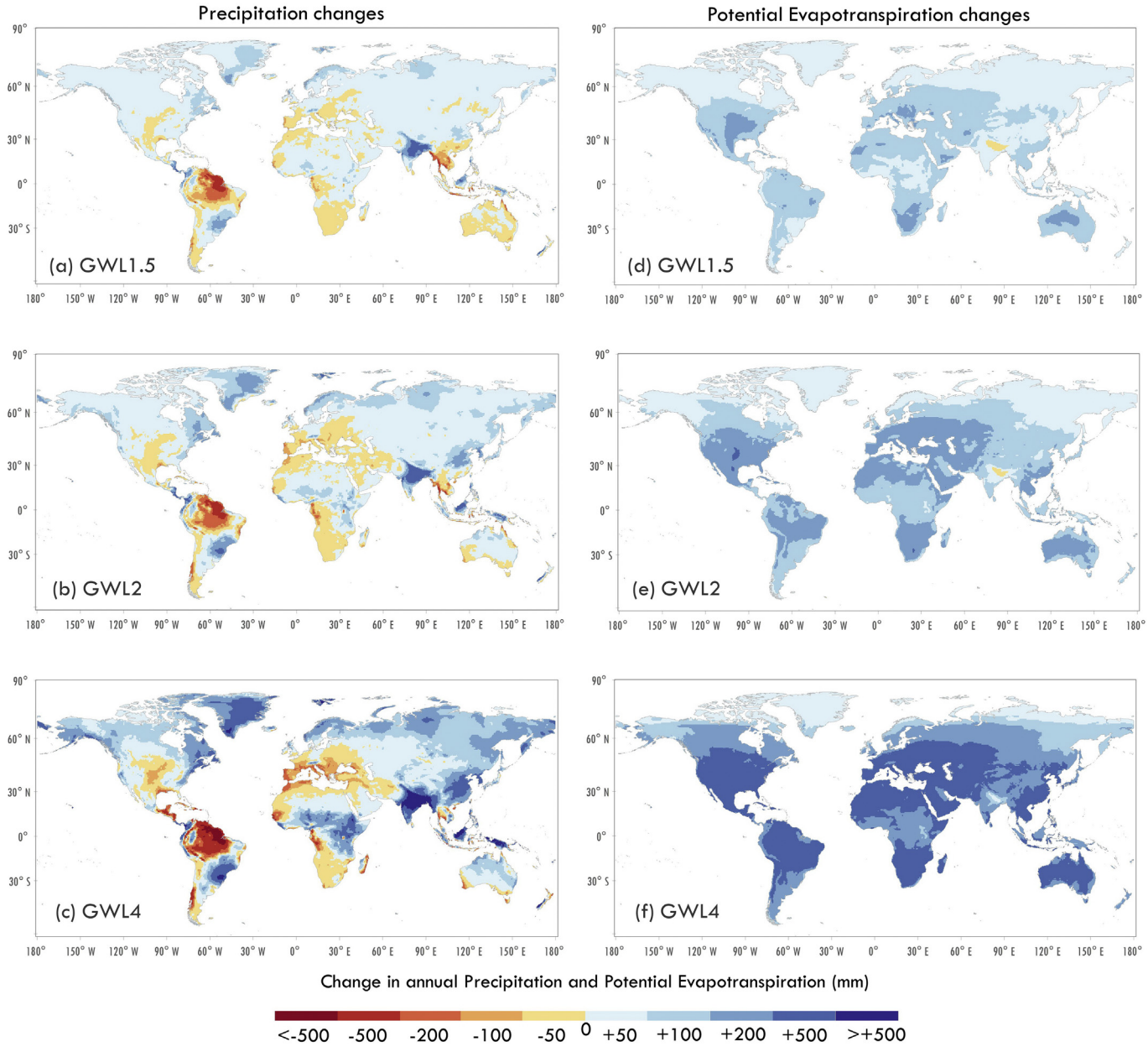


**Fig. A1.** Projected changes in precipitation and potential evapotranspiration for the three specific GWLs relative to the baseline (1981–2010). Values are multi-model mean changes under RCP8.5

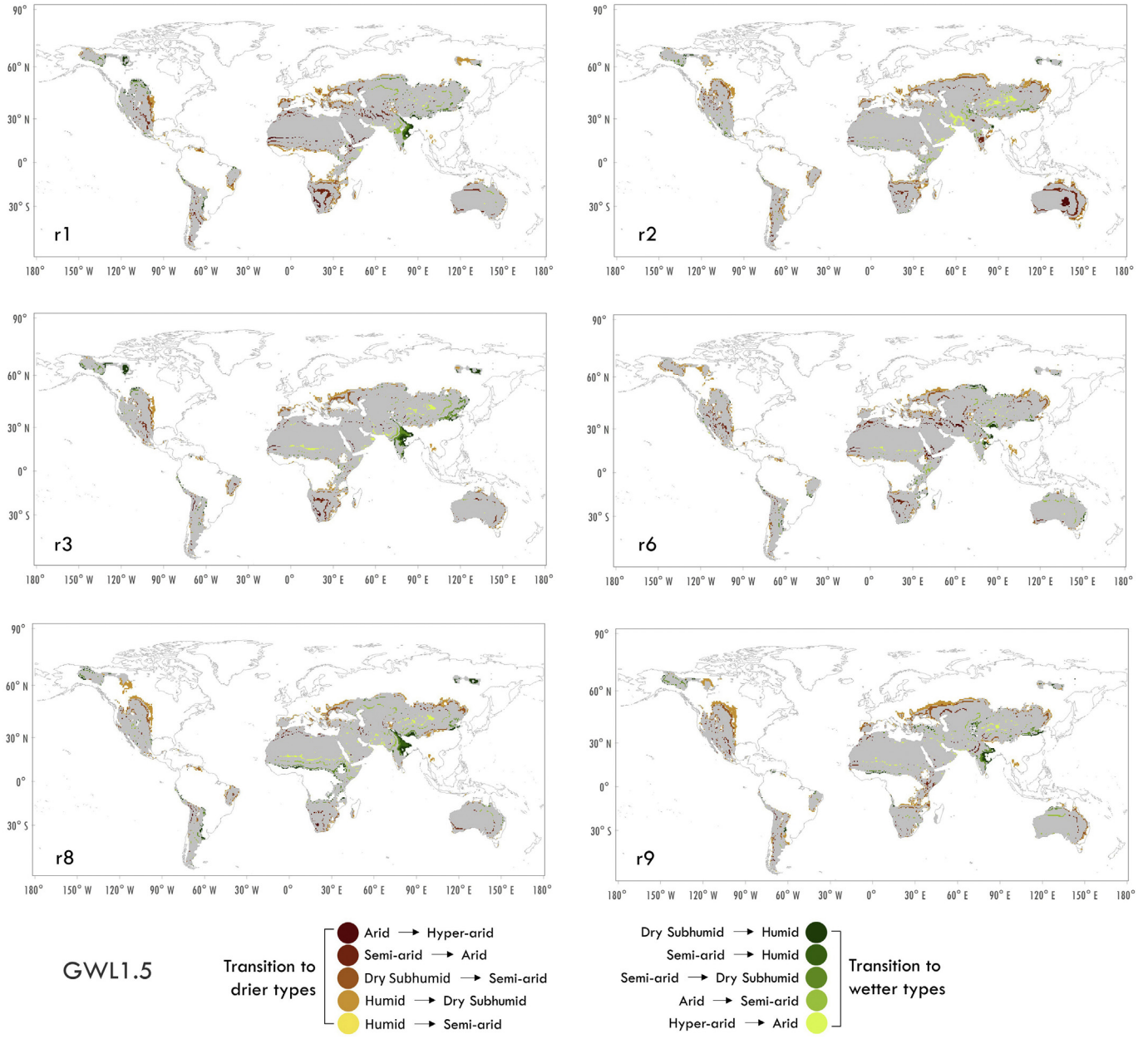


**Fig. A2.** Global distribution of projected drylands transitions according to RCP8.5 for the GWL1.5 relative to the baseline (1981–2010) period. Brown colored areas denote transition to drier types and green colored areas transitions to wetter types. Grey shaded areas are drylands of the baseline period.

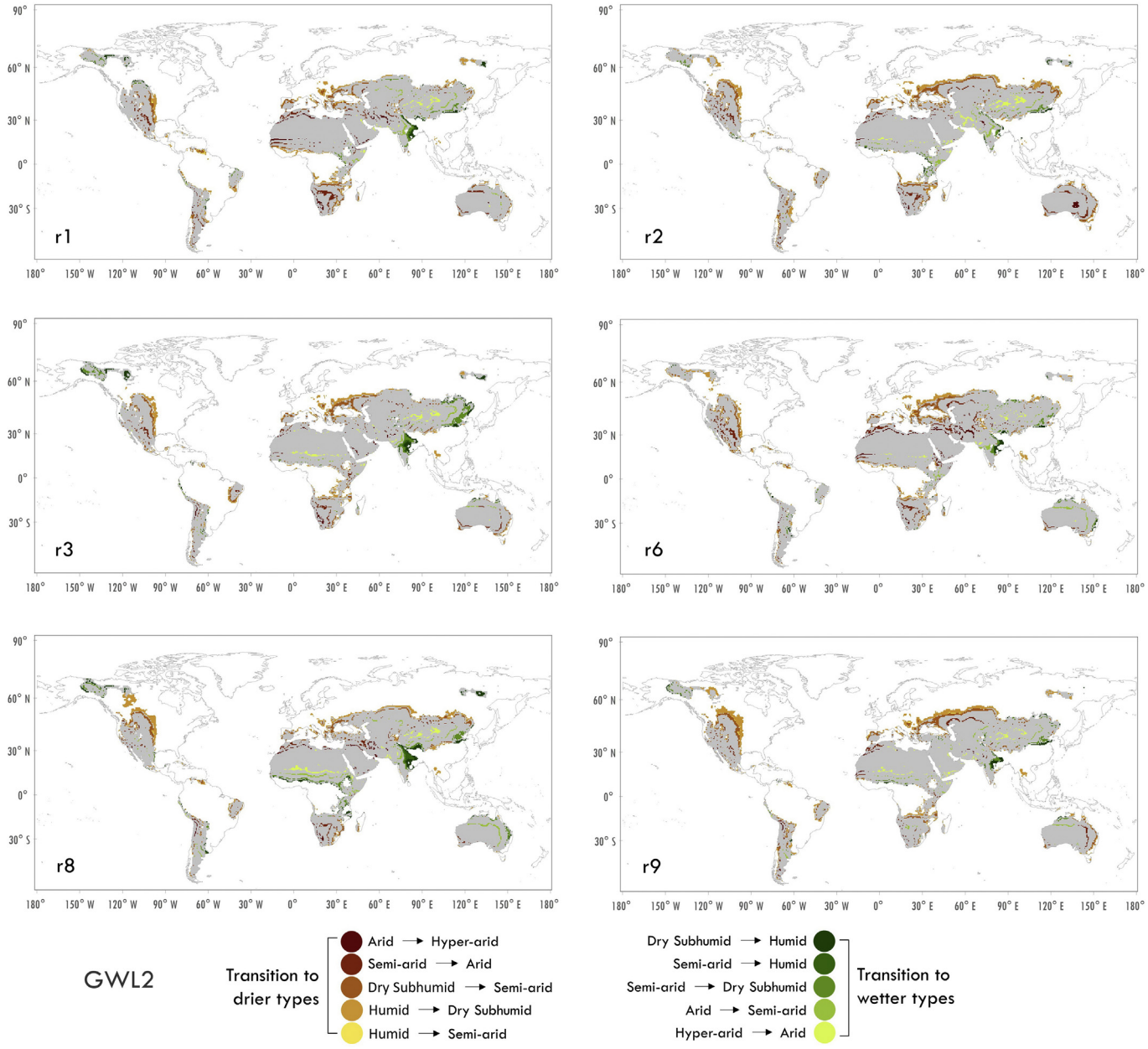


**Fig. A3.** Same as Fig. A2 but for GWL2.

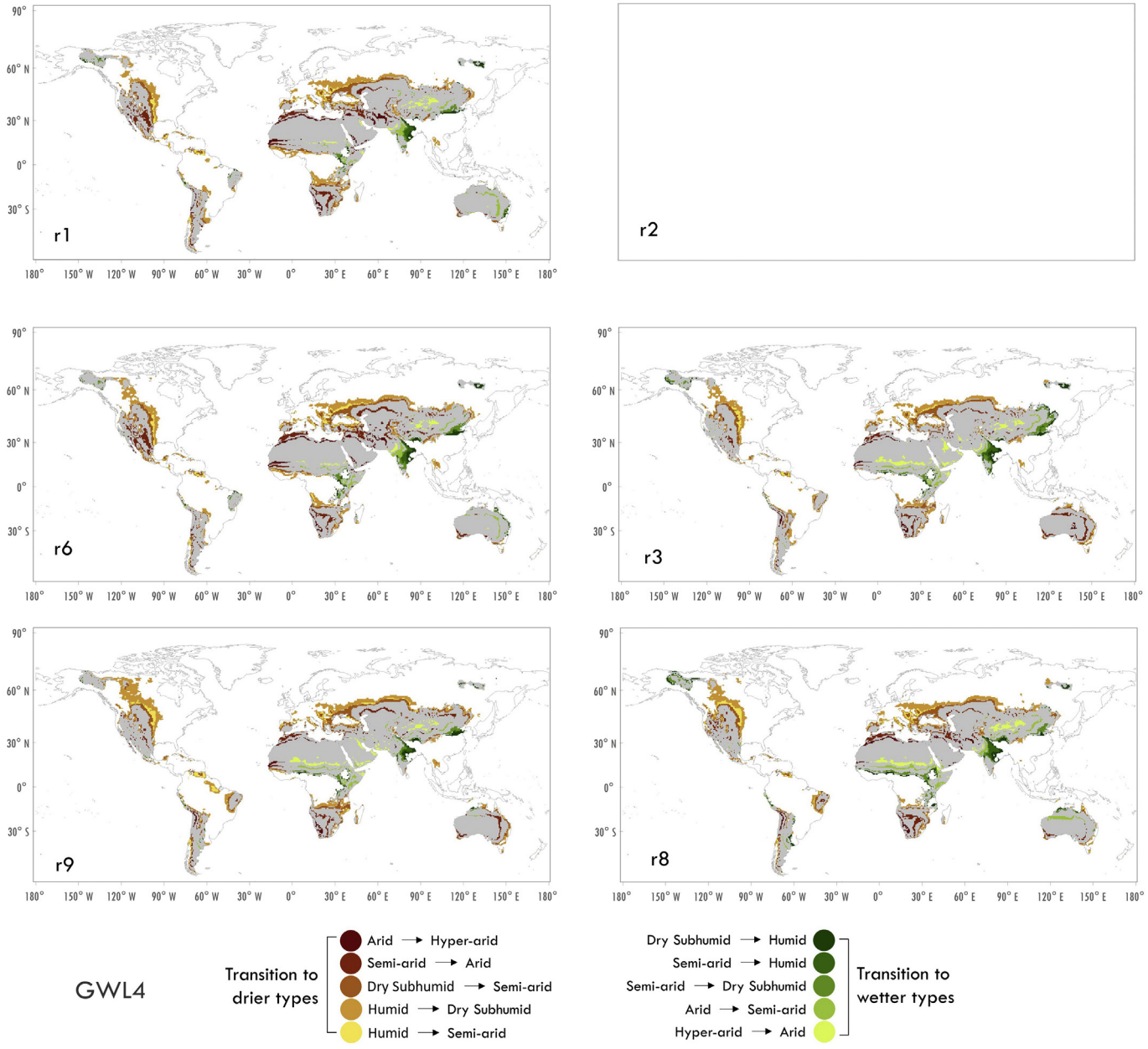


**Fig. A4.** Same as Fig. A2 but for GWL4. (Member r2 - GFDL-ESM2M is not reaching the GWL4).

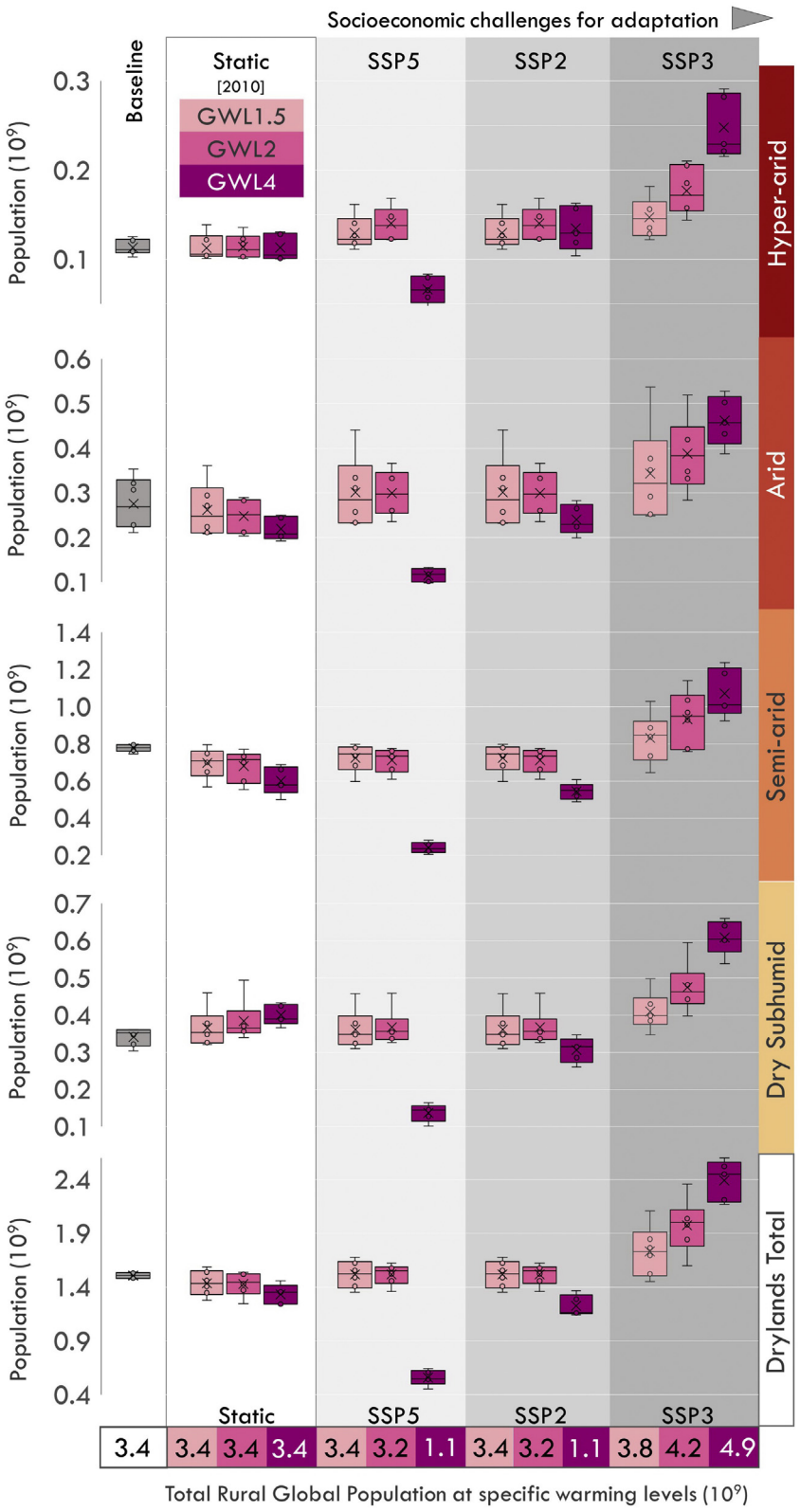


**Fig. A5.** Same as Fig. 7 but for rural population.

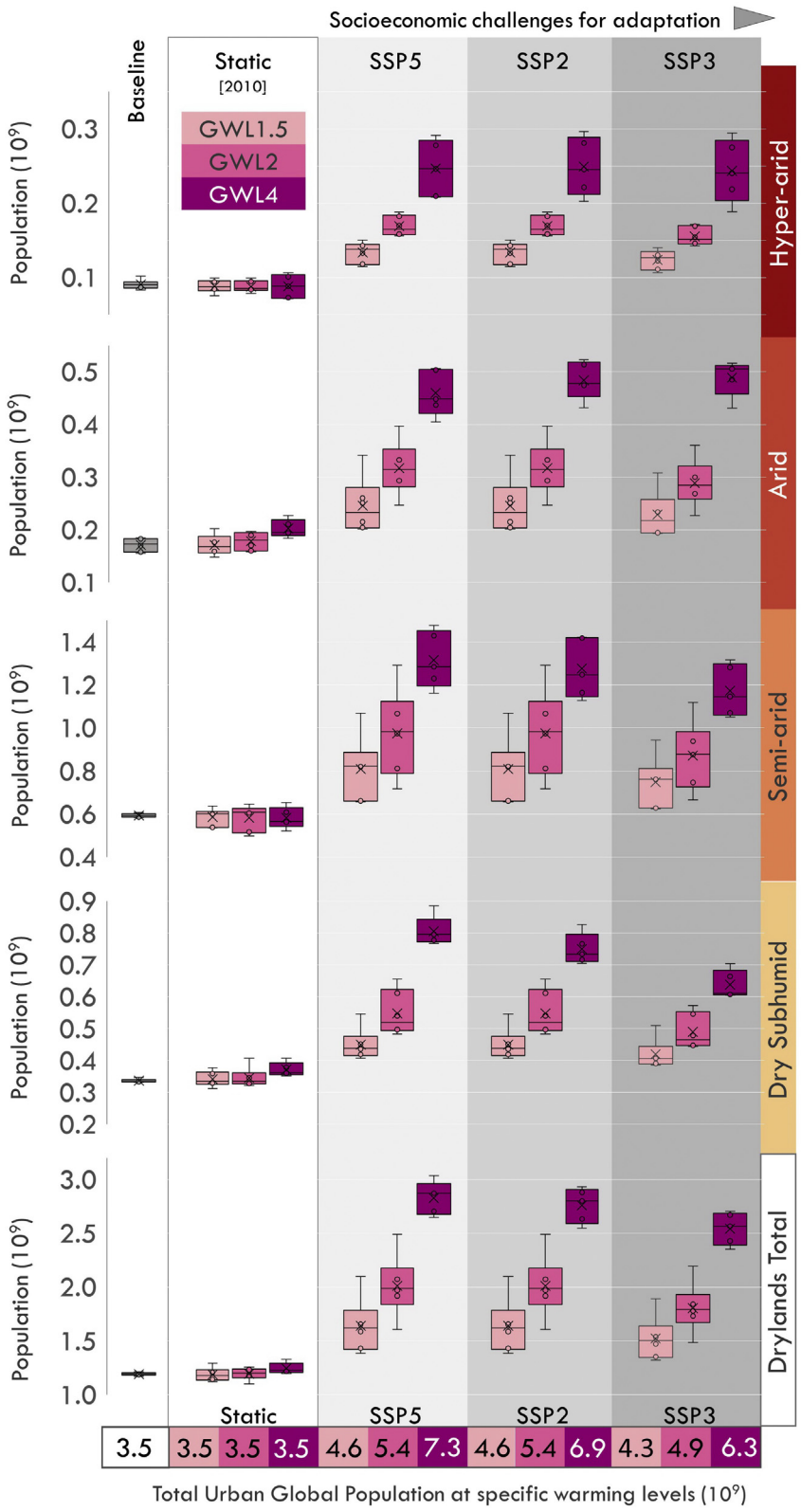


**Fig. A6.** Same as Fig. 7 but for urban population.

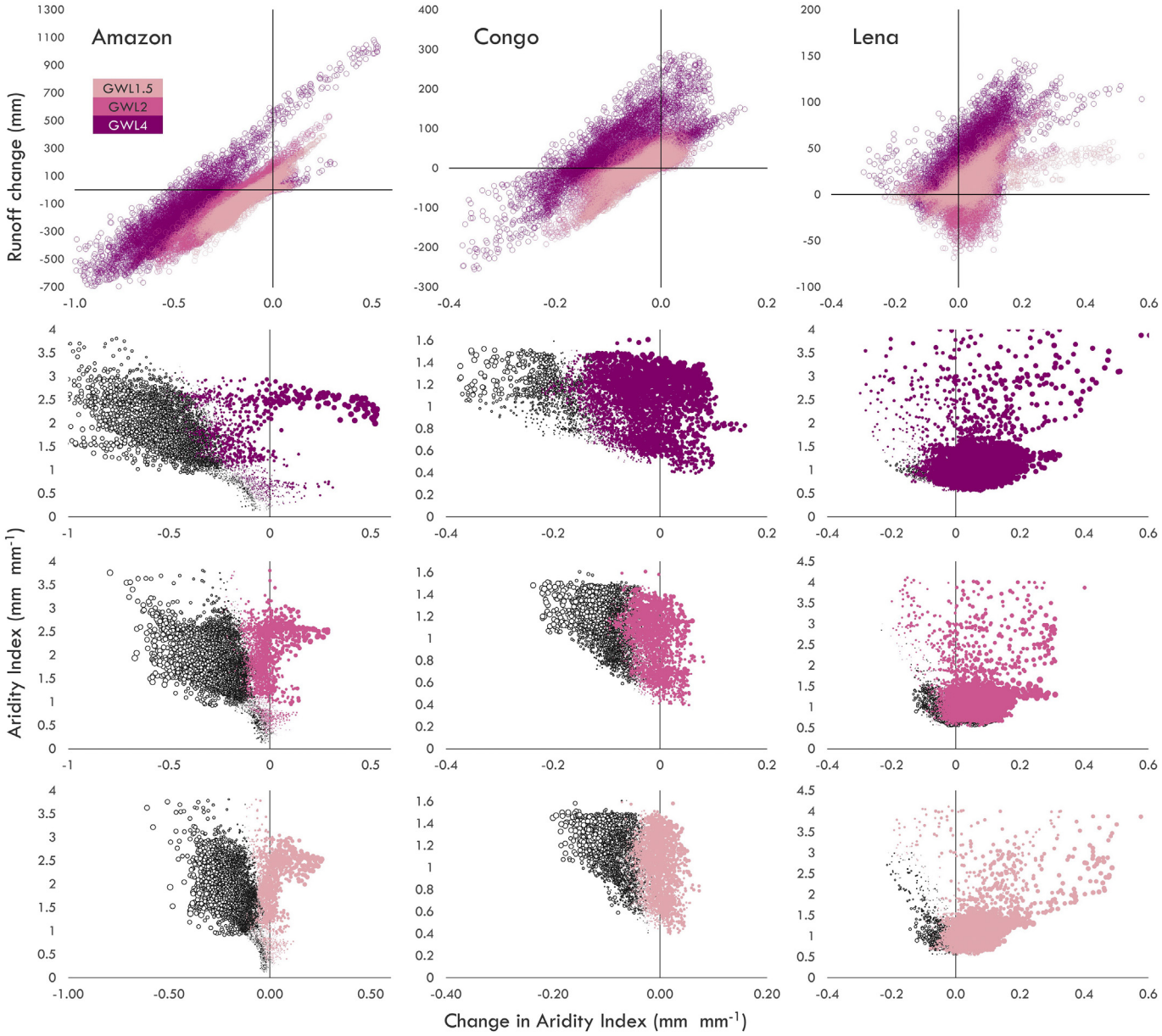


**Fig. A7.** Same as Fig. 11 but for Amazon, Congo and Lena.

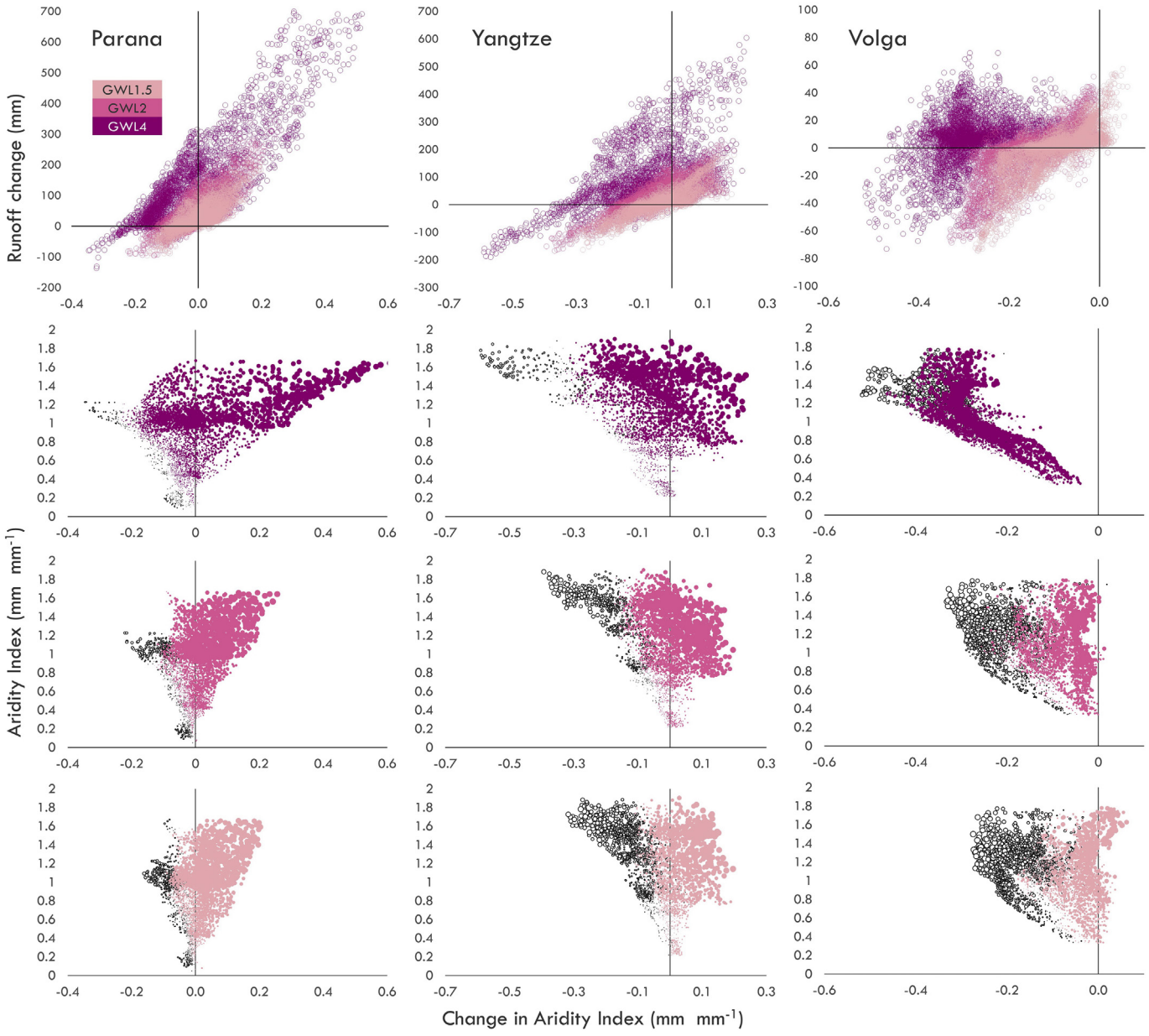


**Fig. A8.** Same as Fig. 11 but for Parana, Yangtze and Volga.

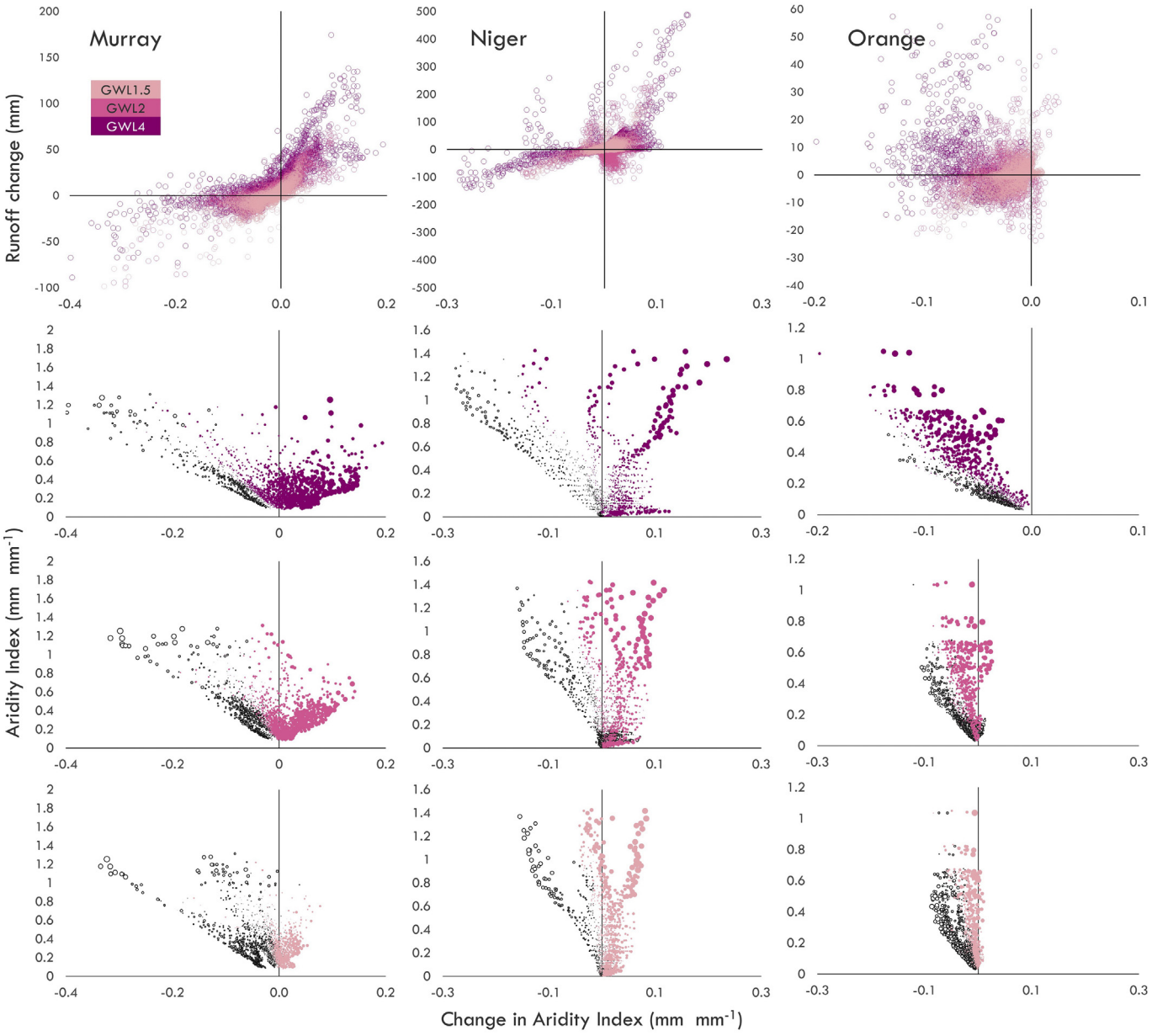


**Fig. A9.** Same as Fig. 11 but for Murray, Niger and Ornage.

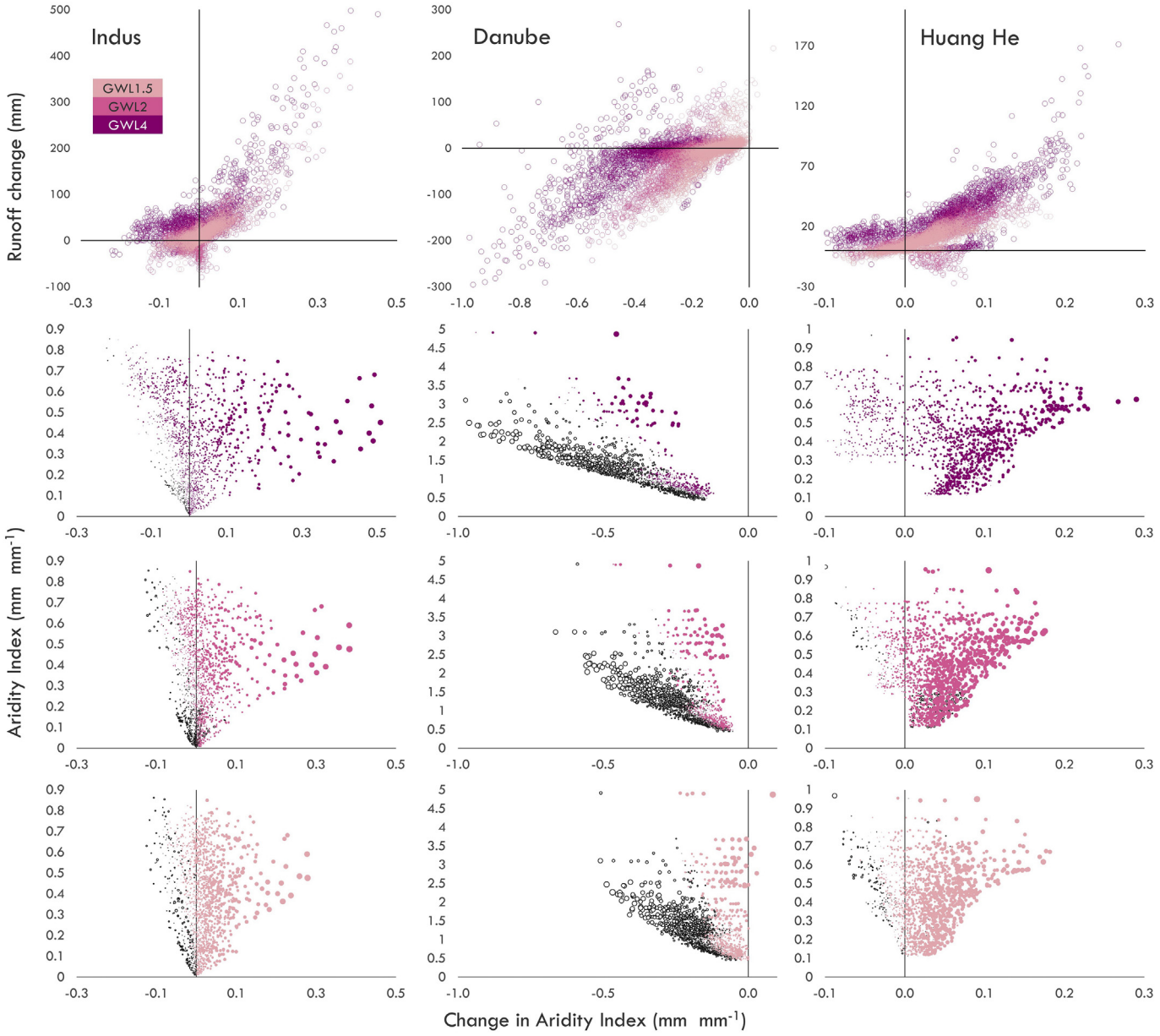


**Fig. A10.** Same as Fig. 11 but for Indus, Danube and Huang He.

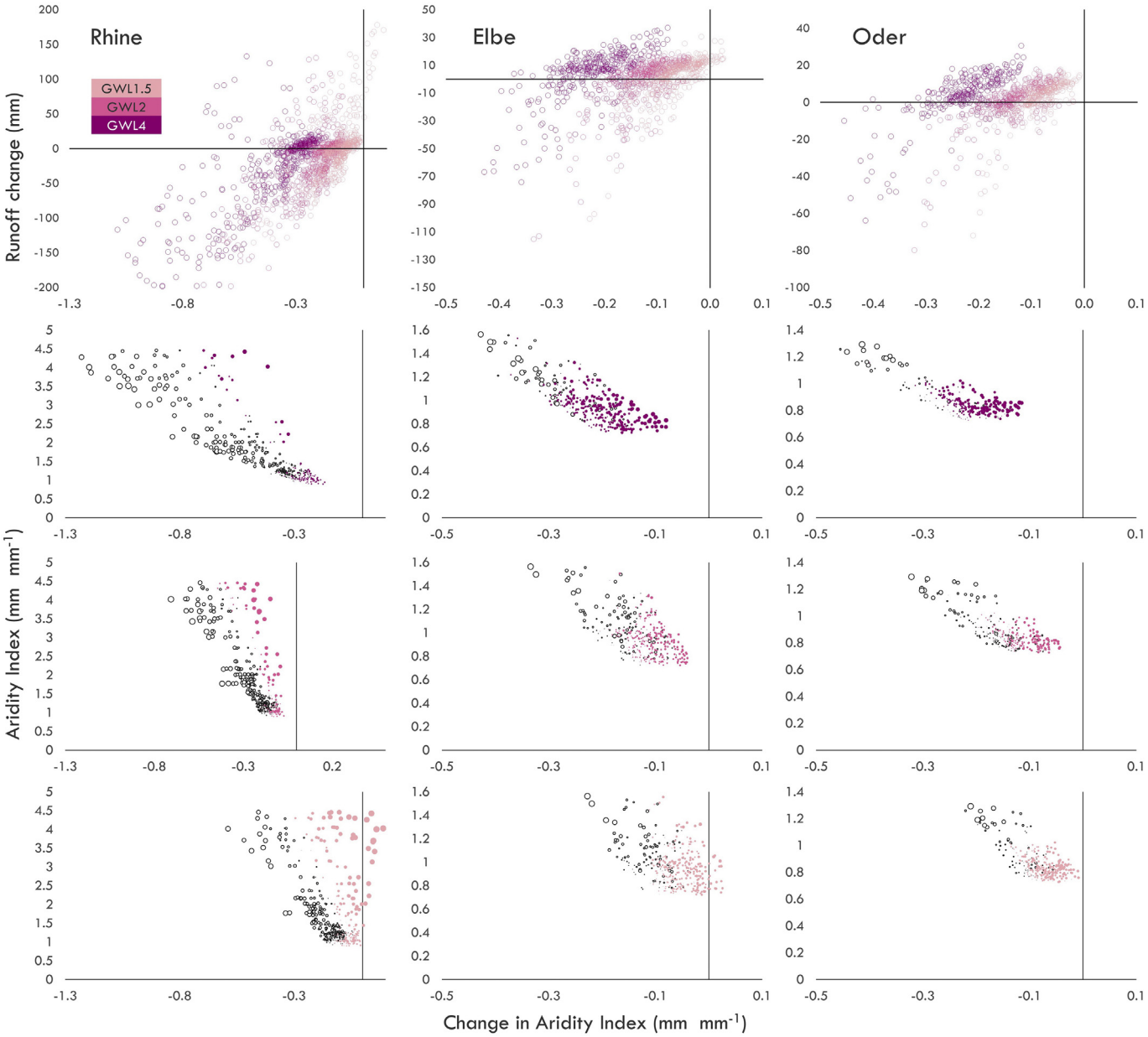


**Fig. A11.** Same as Fig. 11 but for Rhine, Elbe and Oder.

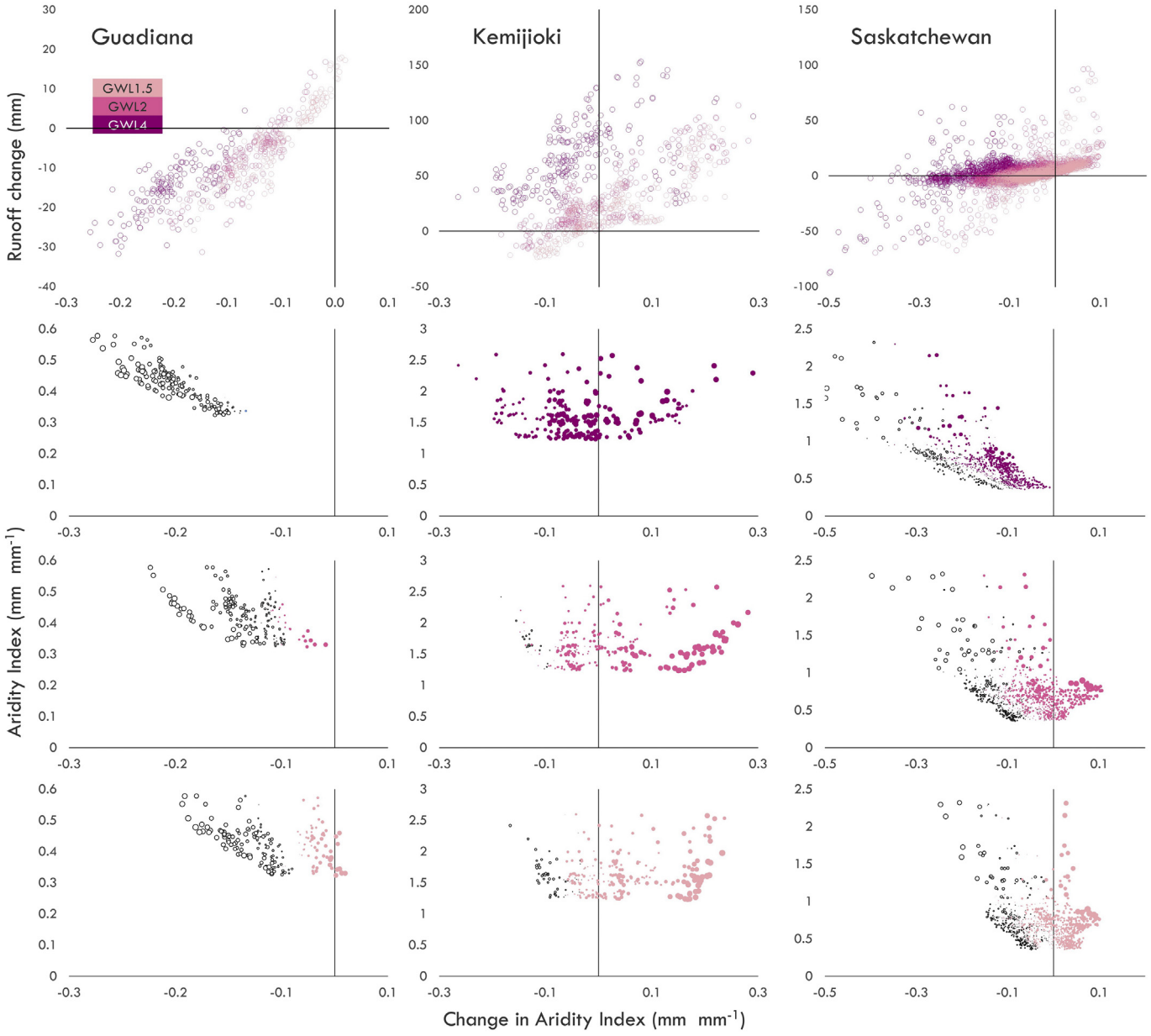


**Fig. A12.** Same as Fig. 11 but for Guadiana, Kemijoki and Saskatchewan.

## References


Alfieri, L., Bisselink, B., Dottori, F., Naumann, G., de Roo, A., Salamon, P., Wyser, K., Feyen, L., 2017. Global projections of river flood risk in a warmer world. Earth's Future 5, 171–182. https://doi.org/10.1002/2016EF000485.

Allen, R.G., Pereira, L.S., Raes, D., Smith, M., 1998. Crop evapotranspiration—guidelines for computing crop water requirements. FAO Irrigation and Drainage Paper 56 300. FAO, Rome, p. 6541.

Asadi Zarch, M.A., Sivakumar, B., Malekinezhad, H., Sharma, A., 2017. Future aridity under conditions of global climate change. J. Hydrol. 554, 451–469. https://doi.org/10.1016/J.JHYDROL.2017.08.043.

Berg, A., Findell, K., Lintner, B., Giannini, A., Seneviratne, S.I., van den Hurk, B., Lorenz, R., Pitman, A., Hagemann, S., Meier, A., Cheruy, F., Ducharne, A., Malyshev, S., Milly, P.C.D., 2016. Land–atmosphere feedbacks amplify aridity increase over land under global warming. Nat. Clim. Chang. 6, 869–874. https://doi.org/10.1038/nclimate3029.

Best, M.J., Pryor, M., Clark, D.B., Rooney, G.G., Essery, R..L.H., Ménard, C.B., Edwards, J.M., Hendry, M.a., Porson, a., Gedney, N., Mercado, L.M., Sitch, S., Blyth, E., Boucher, O., Cox, P.M., Grimmond, C.S.B., Harding, R.J., 2011. The joint UK land environment simulator (JULES), model description — part 1: energy and water fluxes. Geosci. Model Dev. 4, 677–699. https://doi.org/10.5194/gmd-4-677-2011.

Betts, R.A., Golding, N., Gonzalez, P., Gornall, J., Kahana, R., Kay, G., Mitchell, L., Wiltshire, A., 2015. Climate and land use change impacts on global terrestrial ecosystems and river flows in the HadGEM2-ES Earth system model using the representative concentration pathways. Biogeosci. Discuss. 10, 6171–6223. https://doi.org/10.5194/bg-12-1317-2015.

Betts, R.A., Alfieri, L., Bradshaw, C., Caesar, J., Feyen, L., Friedlingstein, P., Gohar, L., Koutroulis, A., Lewis, K., Morfopoulos, C., Papadimitriou, L., Richardson, K.J., Tsanis, I., Wyser, K., 2018. Changes in climate extremes, fresh water availability and vulnerability to food insecurity projected at 1.5 °C and 2 °C global warming with a higher-resolution global climate model. Philos. Trans. R. Soc. A Math. Phys. Eng. Sci. 376. https://doi.org/10.1098/rsta.2016.0452.

Borrelli, P., Robinson, D.A., Fleischer, L.R., Lugato, E., Ballabio, C., Alewell, C., Meusburger, K., Modugno, S., Schütt, B., Ferro, V., Bagarello, V., Van Oost, K., Montanarella, L., Panagos, P., 2017. An assessment of the global impact of 21st century land use change on soil erosion. Nat. Commun. 8, 2013. https://doi.org/10.1038/s41467-017-02142-7.

Budyko, M.I., 1974. Climate and Life. Academic Press, New York, NY, USA.

Chang, J., Ciais, P., Wang, X., Piao, S., Asrar, G., Betts, R., Chevallier, F., Dury, M., François, L., Frieler, K., Ros, A.G.C., Henrot, A.-J., Hickler, T., Ito, A., Morfopoulos, C., Munhoven, G., Nishina, K., Ostberg, S., Pan, S., Peng, S., Rafique, R., Reyer, C., Rödenbeck, C., Schaphoff, S., Steinkamp, J., Tian, H., Viovy, N., Yang, J., Zeng, N., Zhao, F., 2017. Benchmarking carbon fluxes of the ISIMIP2a biome models. Environ. Res. Lett. 12, 045002. https://doi.org/10.1088/1748-9326/aa63fa.

Cherlet, M., Hutchinson, C., Reynolds, J., Sommer, S., von Maltitz, G., 2018. World Atlas of Desertification. Third ed. Publication Office of the European Union, Luxembourg https://doi.org/10.2760/9205.

Dai, A., 2011. Drought under global warming: a review. Wiley Interdiscip. Rev. Clim. Chang. 2, 45–65. https://doi.org/10.1002/wcc.81.

Daliakopoulos, I.N., Tsanis, I.K., Koutroulis, A., Kourgialas, N.N., Varouchakis, A.E., Karatzas, G.P., Ritsema, C.J., 2016. The threat of soil salinity: a European scale review. Sci. Total Environ. 573. https://doi.org/10.1016/j.scitotenv.2016.08.177.

Daliakopoulos, I.N., Panagea, I.S., Tsanis, I.K., Grillakis, M.G., Koutroulis, A.G., Hessel, R., Mayor, A.G., Ritsema, C.J., 2017. Yield response of Mediterranean rangelands under a changing climate. Land Degrad. Dev. 28, 1962–1972. https://doi.org/10.1002/ldr.2717.

Davie, J.C.S., Falloon, P.D., Kahana, R., Dankers, R., Betts, R., Portmann, F.T., Wisser, D., Clark, D.B., Ito, A., Masaki, Y., Nishina, K., Fekete, B., Tessler, Z., Wada, Y., Liu, X., Tang, Q., Hagemann, S., Stacke, T., Pavlick, R., Schaphoff, S., Gosling, S.N., Franssen, W., Arnell, N., 2013. Comparing projections of future changes in runoff from hydrological and biome models in ISI-MIP. Earth Syst. Dyn. 4, 359–374. https://doi.org/10.5194/esd-4-359-2013.

Deser, C., Hurrell, J.W., Phillips, A.S., 2017. The role of the North Atlantic Oscillation in European climate projections. Clim. Dyn. 49, 3141–3157. https://doi.org/10.1007/s00382-016-3502-z.

Dottori, F., Szewczyk, W., Ciscar, J.-C., Zhao, F., Alfieri, L., Hirabayashi, Y., Bianchi, A., Mongelli, I., Frieler, K., Betts, R.A., Feyen, L., 2018. Increased human and economic losses from river flooding with anthropogenic warming. Nat. Clim. Chang. 8, 781–786. https://doi.org/10.1038/s41558-018-0257-z.

Durán, J., Delgado-Baquerizo, M., Dougill, A.J., Guuroh, R.T., Linstädter, A., Thomas, A.D., Maestre, F.T., 2018. Temperature and aridity regulate spatial variability of soil multifunctionality in drylands across the globe. Ecology 99, 1184–1193. https://doi.org/10.1002/ecy.2199.

Feng, S., Fu, Q., 2013. Expansion of global drylands under a warming climate. Atmos. Chem. Phys. 13, 10081–10094. https://doi.org/10.5194/acp-13-10081-2013.

Greve, P., Seneviratne, S.I., 2015. Assessment of future changes in water availability and aridity. Geophys. Res. Lett. 42, 5493–5499. https://doi.org/10.1002/2015GL064127.

Greve, P., Orlowsky, B., Mueller, B., Sheffield, J., Reichstein, M., Seneviratne, S.I., 2014. Global assessment of trends in wetting and drying over land. Nat. Geosci. 7, 716–721. https://doi.org/10.1038/ngeo2247.

Greve, P., Roderick, M.L., Seneviratne, S.I., 2017. Simulated changes in aridity from the last glacial maximum to 4x$CO_2$. Environ. Res. Lett. 12, 114021. https://doi.org/10.1088/1748-9326/aa89a3.

Grillakis, M.G., Koutroulis, A.G., Tsanis, I.K., 2013. Multisegment statistical bias correction of daily GCM precipitation output. J. Geophys. Res. Atmos. 118. https://doi.org/10.1002/jgrd.50323.

Grillakis, M.G., Koutroulis, A.G., Papadimitriou, L.V., Daliakopoulos, I.N., Tsanis, I.K., 2016. Climate-induced shifts in global soil temperature regimes. Soil Sci. 181, 264–272. https://doi.org/10.1097/SS.0000000000000156.

Grillakis, M.G., Koutroulis, A.G., Daliakopoulos, I.N., Tsanis, I.K., 2017. A method to preserve trends in quantile mapping bias correction of climate modeled temperature. Earth Syst. Dyn. 8, 889–900. https://doi.org/10.5194/esd-8-889-2017.

Gudmundsson, L., Greve, P., Seneviratne, S.I., 2016. The sensitivity of water availability to changes in the aridity index and other factors—a probabilistic analysis in the Budyko space. Geophys. Res. Lett. 43, 6985–6994. https://doi.org/10.1002/2016GL069763.

Hawkins, E., Sutton, R., 2011. The potential to narrow uncertainty in projections of regional precipitation change. Clim. Dyn. 37, 407–418. https://doi.org/10.1007/s00382-010-0810-6.

Hempel, S., Frieler, K., Warszawski, L., Schewe, J., Piontek, F., 2013. A trend-preserving bias correction — the ISI-MIP approach. Earth Syst. Dyn. 4, 219–236. https://doi.org/10.5194/esd-4-219-2013.

Hewitt, H.T., Copsey, D., Culverwell, I.D., Harris, C.M., Hill, R.S.R., Keen, A.B., McLaren, A.J., Hunke, E.C., 2011. Design and implementation of the infrastructure of HadGEM3: the next-generation Met Office climate modelling system. Geosci. Model Dev. 4, 223–253. https://doi.org/10.5194/gmd-4-223-2011.

Huang, J., Yu, H., Guan, X., Wang, G., Guo, R., 2016. Accelerated dryland expansion under climate change. Nat. Clim. Chang. 6, 166–171. https://doi.org/10.1038/nclimate2837.

Huang, J., Li, Y., Fu, C., Chen, F., Fu, Q., Dai, A., Shinoda, M., Ma, Z., Guo, W., Li, Z., Zhang, L., Liu, Y., Yu, H., He, Y., Xie, Y., Guan, X., Ji, M., Lin, L., Wang, S., Yan, H., Wang, G., 2017a. Dryland climate change: recent progress and challenges. Rev. Geophys. 55, 719–778. https://doi.org/10.1002/2016RG000550.

Huang, J., Yu, H., Dai, A., Wei, Y., Kang, L., 2017b. Drylands face potential threat under 2 °C global warming target. Nat. Clim. Chang. 7, 417–422. https://doi.org/10.1038/nclimate3275.

Hulme, M., 1996. Recent climatic change in the world's drylands. Geophys. Res. Lett. 23, 61–64. https://doi.org/10.1029/95GL03586.

Jacob, D., Elizalde, A., Haensler, A., Hagemann, S., Kumar, P., Podzun, R., Rechid, D., Remedio, A.R., Saeed, F., Sieck, K., Teichmann, C., Wilhelm, C., 2012. Assessing the transferability of the regional climate model REMO to different COordinated regional climate downscaling EXperiment (CORDEX) regions. Atmosphere (Basel) 3, 181–199. https://doi.org/10.3390/atmos3010181.

Jacob, D., Kotova, L., Teichmann, C., Sobolowski, S.P., Vautard, R., Donnelly, C., Koutroulis, A.G., Grillakis, M.G., Tsanis, I.K., Damm, A., Sakalli, A., van Vliet, M.T.H., 2018. Climate impacts in Europe under +1.5 °C global warming. Earth's Future https://doi.org/10.1002/2017EF000710.

Jones, B., O'Neill, B.C., 2016. Spatially explicit global population scenarios consistent with the Shared Socioeconomic Pathways. Environ. Res. Lett. 11, 084003. https://doi.org/10.1088/1748-9326/11/8/084003.

Knight, J.R., Andrews, M.B., Smith, D.M., Arribas, A., Colman, A.W., Dunstone, N.J., Eade, R., Hermanson, L., MacLachlan, C., Peterson, K.A., Scaife, A.A., Williams, A., Knight, J.R., Andrews, M.B., Smith, D.M., Arribas, A., Colman, A.W., Dunstone, N.J., Eade, R., Hermanson, L., MacLachlan, C., Peterson, K.A., Scaife, A.A., Williams, A., 2014. Predictions of climate several years ahead using an improved decadal prediction system. J. Clim. 27, 7550–7567. https://doi.org/10.1175/JCLI-D-14-00069.1.

Koutroulis, A.G., Grillakis, M.G., Tsanis, I.K., Papadimitriou, L., 2016. Evaluation of precipitation and temperature simulation performance of the CMIP3 and CMIP5 historical experiments. Clim. Dyn. 47, 1881–1898. https://doi.org/10.1007/s00382-015-2938-x.

Koutroulis, A.G., Papadimitriou, L.V., Grillakis, M.G., Tsanis, I.K., Wyser, K., Betts, R.A., 2018a. Freshwater vulnerability under high end climate change. A pan-European assessment. Sci. Total Environ., 613–614 https://doi.org/10.1016/j.scitotenv.2017.09.074.

Koutroulis, A.G., Papadimitriou, L.V., Grillakis, M.G., Tsanis, I.K., Wyser, K., Caesar, J., Betts, R.A., 2018b. Simulating hydrological impacts under climate change: implications from methodological differences of a Pan European assessment. Water (Switzerland) 10, 1331. https://doi.org/10.3390/w10101331.

Meybeck, M., Kummu, M., Dürr, H.H., 2013. Global hydrobelts and hydroregions: improved reporting scale for water-related issues? Hydrol. Earth Syst. Sci. 17, 1093–1111. https://doi.org/10.5194/hess-17-1093-2013.

Milly, P.C.D., Dunne, K.A., 2016. Potential evapotranspiration and continental drying. Nat. Clim. Chang. 6, 946–949. https://doi.org/10.1038/nclimate3046.

Müller Schmied, H., Adam, L., Eisner, S., Fink, G., Flörke, M., Kim, H., Oki, T., Portmann, F.T., Reinecke, R., Riedel, C., Song, Q., Zhang, J., Döll, P., 2016a. Variations of global and continental water balance components as impacted by climate forcing uncertainty and human water use. Hydrol. Earth Syst. Sci. 20, 2877–2898. https://doi.org/10.5194/hess-20-2877-2016.

Müller Schmied, H., Müller, R., Sanchez-Lorenzo, A., Ahrens, B., Wild, M., 2016b. Evaluation of radiation components in a global freshwater model with station-based observations. Water 8, 450. https://doi.org/10.3390/w8100450.

Naumann, G., Alfieri, L., Wyser, K., Mentaschi, L., Betts, R.A., Carrao, H., Spinoni, J., Vogt, J., Feyen, L., 2018. Global changes in drought conditions under different levels of warming. Geophys. Res. Lett. 45, 3285–3296. https://doi.org/10.1002/2017GL076521.

Nicholson, S.E., 2011. Dryland Climatology. Cambridge University Press.

Panagos, P., Borrelli, P., Poesen, J., Ballabio, C., Lugato, E., Meusburger, K., Montanarella, L., Alewell, C., 2015. The new assessment of soil loss by water erosion in Europe. Environ. Sci. Pol. 54, 438–447. https://doi.org/10.1016/J.ENVSCI.2015.08.012.

Papadimitriou, L.V., Koutroulis, A.G., Grillakis, M.G., Tsanis, I.K., 2016. High-end climate change impact on European runoff and low flows — exploring the effects of forcing biases. Hydrol. Earth Syst. Sci. 20, 1785–1808. https://doi.org/10.5194/hess-20-1785-2016.

Papadimitriou, L.V., Koutroulis, A.G., Grillakis, M.G., Tsanis, I.K., 2017. The effect of GCM biases on global runoff simulations of a land surface model. Hydrol. Earth Syst. Sci. 21, 4379–4401. https://doi.org/10.5194/hess-21-4379-2017.

Roderick, M.L., Farquhar, G.D., 2011. A simple framework for relating variations in runoff to variations in climatic conditions and catchment properties. Water Resour. Res. 47. https://doi.org/10.1029/2010WR009826.

Roderick, M.L., Greve, P., Farquhar, G.D., 2015. On the assessment of aridity with changes in atmospheric $CO_2$. Water Resour. Res. 51, 5450–5463. https://doi.org/10.1002/2015WR017031.

Scheff, J., Frierson, D.M.W., Scheff, J., Frierson, D.M.W., 2015. Terrestrial aridity and its response to greenhouse warming across CMIP5 climate models. J. Clim. 28, 5583–5600. https://doi.org/10.1175/JCLI-D-14-00480.1.

Schlaepfer, D.R., Bradford, J.B., Lauenroth, W.K., Munson, S.M., Tietjen, B., Hall, S.A., Wilson, S.D., Duniway, M.C., Jia, G., Pyke, D.A., Lkhagva, A., Jamiyansharav, K., 2017. Climate change reduces extent of temperate drylands and intensifies drought in deep soils. Nat. Commun. 8, 14196. https://doi.org/10.1038/ncomms14196.

Shannon, S., Smith, R., Wiltshire, A., Payne, T., Huss, M., Betts, R., Caesar, J., Koutroulis, A., Jones, D., Harrison, S., 2018. Global glacier volume projections under high-end climate change scenarios. Cryosphere Discuss. https://doi.org/10.5194/tc-2018-35.

Sheffield, J., Goteti, G., Wood, E.F., 2006. Development of a 50-year high-resolution global dataset of meteorological forcings for land surface modeling. J. Clim. 19, 3088–3111. https://doi.org/10.1175/JCLI3790.1.

Sheffield, J., Wood, E.F., Roderick, M.L., 2012. Little change in global drought over the past 60 years. Nature 491, 435–438. https://doi.org/10.1038/nature11575.

Swann, A.L.S., Hoffman, F.M., Koven, C.D., Randerson, J.T., 2016. Plant responses to increasing $CO_2$ reduce estimates of climate impacts on drought severity. Proc. Natl. Acad. Sci. U. S. A. 113, 10019–10024. https://doi.org/10.1073/pnas.1604581113.

Trenberth, K.E., Dai, A., van der Schrier, G., Jones, P.D., Barichivich, J., Briffa, K.R., Sheffield, J., 2014. Global warming and changes in drought. Nat. Clim. Chang. 4, 17–22. https://doi.org/10.1038/nclimate2067.

United Nations, 2016. Report of the Conference Parties on its twenty-first session, held in Paris, 30 November to 13 December 2015. Addendum Part Two: Action Taken by the Conference of the Parties at Its Twenty-first Session.

Vautard, R., Christidis, N., Ciavarella, A., Alvarez-Castro, C., Bellprat, O., Christiansen, B., Colfescu, I., Cowan, T., Doblas-Reyes, F., Eden, J., Hauser, M., Hegerl, G., Hempelmann, N., Klehmet, K., Lott, F., Nangini, C., Orth, R., Radanovics, S., Seneviratne, S.I., van Oldenborgh, G.J., Stott, P., Tett, S., Wilcox, L., Yiou, P., 2018. Evaluation of the HadGEM3-A simulations in view of detection and attribution of human influence on extreme events in Europe. Clim. Dyn., 1–24 https://doi.org/10.1007/s00382-018-4183-6.

Veldkamp, T.I.E., Wada, Y., Aerts, J.C.J.H., Döll, P., Gosling, S.N., Liu, J., Masaki, Y., Oki, T., Ostberg, S., Pokhrel, Y., Satoh, Y., Kim, H., Ward, P.J., 2017. Water scarcity hotspots travel downstream due to human interventions in the 20th and 21st century. Nat. Commun. 8. https://doi.org/10.1038/ncomms15697.

Vousdoukas, M.I., Mentaschi, L., Voukouvalas, E., Bianchi, A., Dottori, F., Feyen, L., 2018. Climatic and socioeconomic controls of future coastal flood risk in Europe. Nat. Clim. Chang. 8, 776–780. https://doi.org/10.1038/s41558-018-0260-4.

Walters, D.N., Best, M.J., Bushell, A.C., Copsey, D., Edwards, J.M., Falloon, P.D., Harris, C.M., Lock, A.P., Manners, J.C., Morcrette, C.J., Roberts, M.J., Stratton, R.A., Webster, S., Wilkinson, J.M., Willett, M.R., Boutle, I.A., Earnshaw, P.D., Hill, P.G., MacLachlan, C., Martin, G.M., Moufouma-Okia, W., Palmer, M.D., Petch, J.C., Rooney, G.G., Scaife, A.A., Williams, K.D., 2011. The Met Office Unified Model Global Atmosphere 3.0/3.1 and JULES Global Land 3.0/3.1 configurations. Geosci. Model Dev. 4, 919–941. https://doi.org/10.5194/gmd-4-919-2011.

Williams, A.P., Allen, C.D., Millar, C.I., Swetnam, T.W., Michaelsen, J., Still, C.J., Leavitt, S.W., 2010. Forest responses to increasing aridity and warmth in the southwestern United States. Proc. Natl. Acad. Sci. U. S. A. 107, 21289–21294. https://doi.org/10.1073/pnas.0914211107.

Wyser, K., Strandberg, G., Caesar, J., Gohar, L., 2016. Documentation of Changes in Climate Variability and Extremes Simulated by the HELIX AGCMs at the 3 SWLs and Comparison in Equivalent SST/SIC Low-resolution CMIP5. HELIX Project Deliverable 3.1. Projections.

Yang, Y., Zhang, S., McVicar, T.R., Beck, H.E., Zhang, Y., Liu, B., 2018. Disconnection between trends of atmospheric drying and continental runoff. Water Resour. Res. 54, 4700–4713. https://doi.org/10.1029/2018WR022593.